Journal of Materials Research and Technology 27 (2023) 6192–6210

Contents lists available at ScienceDirect

Journal of Materials Research and Technology

journal homepage: www.elsevier.com/locate/jmrt

In-plane quasi-static compression deformation of Ti6Al4V double arrow-headed lattice structures fabricated by electron beam powder bed fusion process: Build orientation, scan speed and failure mechanism

Zana Eren [a,*], Ozkan Gokcekaya [b,c,**], Takayoshi Nakano [b,c], Zahit Mecitoğlu [a]

[a] Faculty of Aeronautics and Astronautics, Istanbul Technical University, Istanbul, 34367, Turkey
[b] Division of Materials and Manufacturing Science, Graduate School of Engineering, Osaka University, 2-1, Yamadaoka, Suita, Osaka, 565-0871, Japan
[c] Anisotropic Design & Additive Manufacturing Research Center, Osaka University, 2-1, Yamadaoka, Suita, Osaka, 565-0871, Japan

ARTICLE INFO

Keywords:
Mechanical metamaterials
Electron beam powder bed fusion process
Double arrow-headed lattice
Compression deformation
Microstructure

ABSTRACT

The 2D double arrow-headed (DAH) lattice structures, which are promising cellular structures for impact mitigation, remain relatively unexplored in terms of their compression response when manufactured using the powder bed fusion process with Ti6Al4V (Ti64) alloy. This study aims to investigate the effects of build orientation and beam scan speed of Electron Beam Powder Bed Fusion (PBF-EB) process on the energy absorption of 2D Ti64 DAH lattice structures. Additionally, potential microstructural variations due to adjusted process parameters can be linked to different levels of energy absorption. For the compressions, the lattice structures were manufactured at two build orientations (0° and 45°), using three different beam scan speeds: speed function (SF), low speed (LS), high speed (HS). In micro-characterizations, the unit cells of 0deg-LS exhibited the lowest microporosity level at 0.12 %. Based on KAM values, thin struts at unit cells had higher residual stresses than thick struts, contributing to the initiation of failure locations. The compressions revealed that the 0deg-LS group absorbed 21.6 % and 24 % more energy than 0deg-SF and 0deg-HS groups, respectively, at compressions of 33 %. 45° samples absorbed approximately 10 % more energy than 0° samples except HS groups. The lowest microporosity of 0deg-LS contributed to having the highest energy absorption among 0deg samples. As the residual stresses in KAM values did not differ strongly with varying beam speed, varied energy absorptions were not linked to them. An optimization of the numerical compressions helped obtain designs with higher energy absorption and less relative volume. This study provides valuable insights into Ti64 cellular applications constrained with 2D-type designs.

1. Introduction

Engineering structures in the aerospace and defense industries require lightweight cellular designs to achieve enhanced performance, including impact mitigation, vibration attenuation, crash load absorption, and effective thermal cooling. Additive manufacturing techniques make it possible to manufacture advanced cellular designs. In this context, auxetic lattice structures, which are mechanical metamaterials exhibiting a negative Poisson's ratio, show promise in improving mechanical properties through suitable geometrical manipulations [1–3]. Various researchers have investigated and proposed different lattice structures based mechanical metamaterials, such as designs from chiral or re-entrant families, to explore their performance boundaries [4–7]. There are also recent attempts developed modified new auxetic lattice structures to enhance crushing energy absorption [8,9]. Fig. 1 illustrates examples of topologies, including a conventional 2D lattice structure (hexagonal honeycomb) and non-conventional ones, which are metamaterials based on 2D lattice structures (re-entrant, anti-tetrachiral, and double arrow-headed (DAH) lattices, respectively). The topologies shown in Fig. 1-a are extruded in the direction normal to the page, classifying them as 2D lattice structures [10]. In this configuration, their in-plane directions are defined as the x and y axes, while the out-of-plane direction points towards the page's normal. Geometrical manipulations within the x-y plane can modify their in-plane stiffness, strength,

* Corresponding author.
** Corresponding author. Division of Materials and Manufacturing Science, Graduate School of Engineering, Osaka University, 2-1, Yamadaoka, Suita, Osaka, 565-0871, Japan.
E-mail addresses: erenza@itu.edu.tr (Z. Eren), ozkan@mat.eng.osaka-u.ac.jp (O. Gokcekaya).

https://doi.org/10.1016/j.jmrt.2023.11.027
Received 12 July 2023; Received in revised form 17 September 2023; Accepted 2 November 2023
Available online 7 November 2023

Poisson's ratio, and performance in plastic compression. Fig. 1-b depicts in-plane and out-of-plane loadings on a 2D lattice structure, respectively.

A specific case of re-entrant, DAH lattice structures which are expected to exhibit higher compressive stiffness and plateau strength in the in-plane direction, compared to other re-entrant lattice structures, hold promise for energy absorption systems [11]. Qiao and Chen [12], have already numerically investigated the deformation of 2D DAH lattice structures with generic aluminum material data to understand the effects of unit cell angles on energy absorption. They have also derived analytical equations to obtain the elastic modulus, Poisson's ratio, and plateau stress. Recent experimental studies on the compression of DAH lattice structures have focused on their three dimensional (3D) versions. Several authors [13,14], have reported improved specific stiffness or high vibration damping in carbon fiber 3D lattice structures. Among the limited number studies that employed Powder Bed Fusion (PBF) process for manufacturing, Gao et al. [15], investigated the crashworthiness performance of steel 3D DAH lattices with different slenderness ratios to obtain the optimal design for automotive crash-boxes. Yang et al. [16], slightly modified the V shapes in steel 3D DAH lattice structures to U shapes to mitigate stress concentrations. In another study, Yang et al. [17], manufactured 3D re-entrant lattice structures from Ti64 powder using the Electron Beam Powder Bed Fusion (PBF-EB) process and achieved superior performance compared to foam materials. Although 3D lattice structures offer the advantage of reduced weight, the 2D design logic investigated in Ref. [12], may be an necessary for task-related requirements, such as high-temperature fluid flow inside channels or high load bearing applications. Therefore, further understanding of the deformation of 2D lattice structures under compression loads is needed. However, recent studies for the 2D approach have mainly focused on polymeric base materials. Günaydin et al. [18], employed thickened struts between 2D re-entrant lattice columns to prevent separations due to weak strength under the compression, as compared to 2D anti-tetrachiral lattice structures. Choudhry et al. [19], enhanced the in-plane energy absorption of polymeric 2D re-entrant lattice structures by modifying geometries. Guo et al. [20], demonstrated that Acrylonitrile Butadiene Styrene (ABS) plastic based cylindrical hollow tubes with 2D re-entrant lattice walls enhance the energy absorption compared to tubes with honeycombs walls. Wang et al. [21], investigated several auxetic designs with concave struts to enhance impact absorption. Zhao et al. [22], studied the compression of Polylactic Acid (PLA) material-based four-*star* DAH lattice structures, which are a hybrid of 2D double arrow headed and 2D star shape lattices. They demonstrated that the concave angle in the unit cell and the number of arrangements strongly influence the deformation shape, and absorbed energy. Xu et al. [23], introduced DAH sub-cells into hierarchical honeycombs to increase the in-plane energy absorptions of the structure. It is important to note that the deformation behavior of specific geometries depends on the base material and the additive manufacturing process due to inherent process specifications. For instance, Arjunan et al. [24], investigated the compressive deformation of AlSi10Mg based 2D re-entrant lattice blocks with different strut thicknesses to achieve stable behavior, and obtained higher elastic and compressive properties based on the manufacturing informed design.

PBF techniques for metals, such as PBF-EB and PBF-L, have garnered specific interest due to their capability to process various types of metal alloys [25]. Both techniques locally melt powders layer by layer using high-power energy sources – electron beams and lasers, respectively – during the manufacturing process. These methods enable the creation of metal microstructures with strength comparable to conventional counterparts [26] and the production of complex cellular structures with a high dimensional accuracy [27,28]. Although there are studies about metal powder reinforced filament or resin based additive manufacturing techniques, these cannot provide mechanical properties comparable to those of PBF parts [29,30]. With the appropriate device configuration, high-power sources provide distinct advantages for melting graded metal powders when manufacturing multi-material parts, as well [31]. The PBF-EB technique, in particular, offers significant benefits. It operates at higher processing temperatures and has lower oxygen levels in the chamber. These conditions result in reduced residual stresses within the manufactured parts and minimize the likelihood of oxidation occurring on the produced components [32]. Furthermore, outcomes from the PBF-EB technique often eliminate the need for post-processing steps to alleviate stress within the components. This aspect proves to be pivotal in enabling faster production cycles within the industry. On the other hand, the parts produced using PBF-L exhibit better surface roughness [33–35], and PBF-L with a thermal post process can be an option to enhance mechanical properties [36]. This is particularly valid

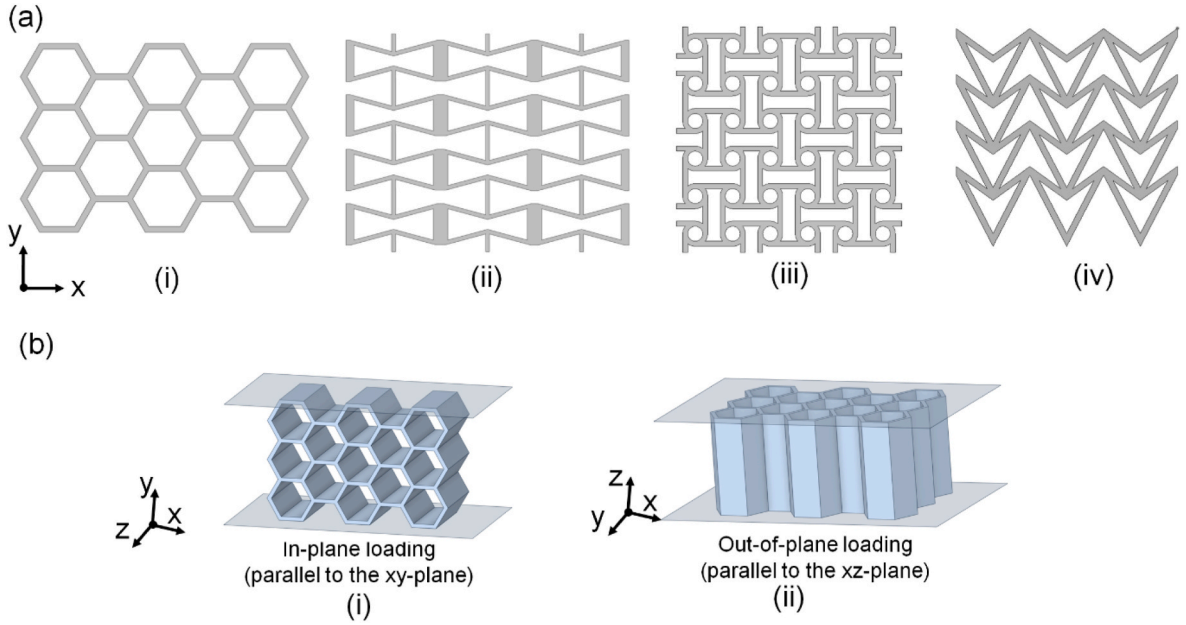

Fig. 1. (a) Example topologies of 2D lattice structures: (i) Hexagonal honeycomb. (ii) Re-entrant (thickened inter-columns). (iii) Anti-tetrachiral. (iv) Double arrow headed. (b) Visual representation of "in-plane" type and "out-of-plane" type loading on a 2D lattice structure.

when shape distortions are limited such as for large sheet-based panels or cellular structures.

The alloy Ti64 is a prominent alloy in the aerospace industry due to its high strength and lightweight nature. However, the manufacturing process using PBF can introduce defects [37,38], micro porosities [39], surface roughness [40], and inherent anisotropy [32,41], which can impact the crushing behavior and failure modes of parts. Cansizoglu et al. [42] obtained that Ti64 lattices manufactured by PBF-EB process in different build orientations exhibited significantly varying compressive strengths. Xiao et al. [43], showed that geometrical and surface irregularities due to the nature of PBF-EB at Ti64 rhombic dodecahedron lattices caused strength reduction, and size effect, particularly specimens under 4 mm in size. Additionally, the response of lattices showed significant discrepancies as they became smaller. Du Plesis et al. [44], revealed that increasing micro-porosities in PBF-L based Ti64 gyroid lattices reduced their strength, with detrimental effect of micro-porosities being more significant than lack of fusion defects. Choy et al. [45], observed different compression failure modes, such as layer by layer, diagonal shear band, V-shape compression/band as relative densities increased in Ti64 3D cubic and honeycomb lattice structures (different lattice diameters). Designs with low relative densities compressed layer by layer, while those with higher relative densities exhibited diagonal band and crack-based formations. Ataee et al. [46], manufactured Ti64 gyroid scaffolds using the PBF-EB with three different unit cell sizes (1 mm, 2 mm and 3 mm) for bone implementations. They found that while the lattices exhibited higher strength in the build direction than in the perpendicular direction, the responses of the design with unit cells of 3 mm were very similar to each other. Moreover, both brittle and ductile compressive formations were observed simultaneously. Yang et al. [17], identified two failure modes in PBF-EB printed 3D re-entrant lattice structures that appeared to depend on the ratio between the lengths of vertical and re-entrant struts. Li et al. [47], observed that Ti64 FCCZ and BCCZ lattices exhibited different failure modes under compressive load. BCCZ lattices experienced failures in the form of buckling, while FCCZ lattices exhibited abrupt shear failures. Guercio et al. [48], found a close correlation between the absorbed compression energy of Ti64 X-type lattices manufactured using PBF-EB and relative densities. Ikeo et al. [49], investigated the compression response of Ti64 honeycomb filled with powder, where they obtained reduced stress concentration at the struts and an extended plateau region. Additionally, Kotzem et al. [50], manufactured F2CCZ and BCC type geometries using the PBF-EB process with Ti64 material. They observed that different microstructural features contributed to achieving more ductile behavior in BCC lattices, while F2CCZ lattices exhibited higher stiffness and strength. The studies mentioned above summarize the effects of the PBF process on cellular designs. Although high specific stiffness has been reported for 2D DAH lattices, their fabrication using the PBF process has not yet been reported. Furthermore, studies on the PBF-EB process have demonstrated that different process parameters can lead to variations, including anisotropy, levels of defects, and micro-porosities, which can affect the elastic and compressive behaviors of lattice structures. It is also known that Ti64 samples exhibit strong brittle behavior [45,46]. Previous studies on the deformation of polymeric DAH lattices cannot provide insights into the deformation patterns or energy absorption efficiency of lattices using Ti64 powder bed materials. The motivation of this study is to fill the research gap by manufacturing 2D DAH lattices with Ti64 material and examining their energy absorptions and deformation patterns for the first time in the literature, which can be affected by PBF-EB process-related parameters, during the compression deformation. Additionally, the study seeks to develop an accurate finite element analysis of Ti64 2D DAH lattices by understanding of damage behavior/patterns in the compression experiments. By capturing recurring imperfections caused by the PBF process and identifying deformation modes, these effects can be incorporated into the parametric studies through a numerical calibration process.

The present study investigates the compression deformation of 2D DAH lattices fabricated using the PBF-EB and Ti64 powders as an example of 2D lattices. The effects of different scan speeds and build orientations are evaluated under quasi-static compression to determine their effect on the specific energy absorption (SEA) and the force-deflection curve while considering the differences in microstructure of thin and thick struts. Observing the critical buckling or failure locations can provide insight to suggest new designs with enhanced performance. Once the numerical model of the compression is validated, unit-cell angles and thickness are employed as variables to optimize with the objectives of high SEA and low relative volume.

2. Materials and methods

2.1. Design

The DAH unit cells are a type of re-entrant unit cells, exhibiting negative Poisson's ratio under a compressive loading in the y-direction. Their compressive strength or stiffness in the y-direction can be tailored based on in-plane elasticity equations (the x-y plane in Fig. 1 or Fig. 2), as demonstrated in a study by Qiao and Chen [12]. Fig. 2 also shows a unit cell of the DAH lattice structure, where θ_1 and θ_2 represent angles at buckling points.

Eqs. (1) and (2) describe the relation between E_y and θ_1, θ_2. In the equations, σ_∞ is applied stress applied onto the plane at top of the DAH cell, ε_y is normal strain in y-direction. E_c is Young's modulus of the lattice material. b and l represents the depth and the half width of one DAH cell, respectively.

$$E_y = \frac{\sigma_\infty}{\varepsilon_y} = \frac{3E_c I}{bl^3}\alpha(\theta_1, \theta_2) \tag{1}$$

$$\alpha = -\frac{4(\cos\theta_1 - \cos\theta_2)}{\sin\theta_1 \sin\theta_2} - \frac{(\cos\theta_1 \cos\theta_2 - 1)^2(\cos\theta_1 \cos\theta_2 - 3)}{\sin\theta_1 \sin\theta_2(\cos\theta_1 - \cos\theta_2)} + \frac{(\cos\theta_1 \cos\theta_2 + 3)(\cos\theta_1 \cos\theta_2 - 1)}{(\cos\theta_1 - \cos\theta_2)} \tag{2}$$

Here, σ_∞ is applied stress applied onto the plane at top of the DAH cell, ε_y is normal strain in y-direction. E_c is Young's modulus of the lattice material. b and l represents the depth and the half width of one DAH cell, respectively. Analytical equations showed that for a design with $\theta_1 = 60^\circ$, lowering θ_2 values in the range of $10^\circ - 50^\circ$ makes negative Poisson's ratio larger (e.g. $\theta_1 = 60^\circ, \theta_2 = 15$, ϑ_{xy} = -2.25). Similarly, lowering θ_2 values, below 40°, increases Young's modulus. For a design with $\theta_2 = 30^\circ$, lowering θ_1 values makes the negative Poisson's ratio larger (e.g. $\theta_1 = 45^\circ$, ϑ_{xy} = -1.79). Additionally, θ_1 values between $40^\circ - 50^\circ$, increases Young's modulus, while values between $55^\circ - 80^\circ$ has no effect on the modulus. Other options to achieve a high Young's modulus in the y direction (e.g., $\theta_1 = 60^\circ$, $\theta_2 = 15^\circ$ and $\theta_1 = 40^\circ$, $\theta_2 = 30^\circ$) or larger negative Poisson's ratio can be experimentally tested under compression loading. A relationship between energy absorption and Poisson's ratio or Young modulus of the design can contribute to finding the unit cell dimensions tailored for energy absorption under compressive loads. However, driving aspect in the present study is understanding the manufacturing-related effects on the deformation and energy absorption of DAH lattice structures. Based on the analytical equations, numerical results [12] and our preliminary knowledge of the manufacturability, a 5 × 5 lattice block (w = 50 mm, h = 45.1 mm, d = 25 mm) with t = 1 mm, $\theta_1 = 98^\circ$ and $\theta_2 = 62^\circ$, was designed to evaluate the compression response of the structure. The width of the lattice block along the x-axis was set to 50 mm, while its dimension along the z-axis (depth) was chosen as 25 mm. This decision was made to simplify the manufacturing process and to enable the observation of plastic collapses with a reasonable compressive reaction force for the test system.

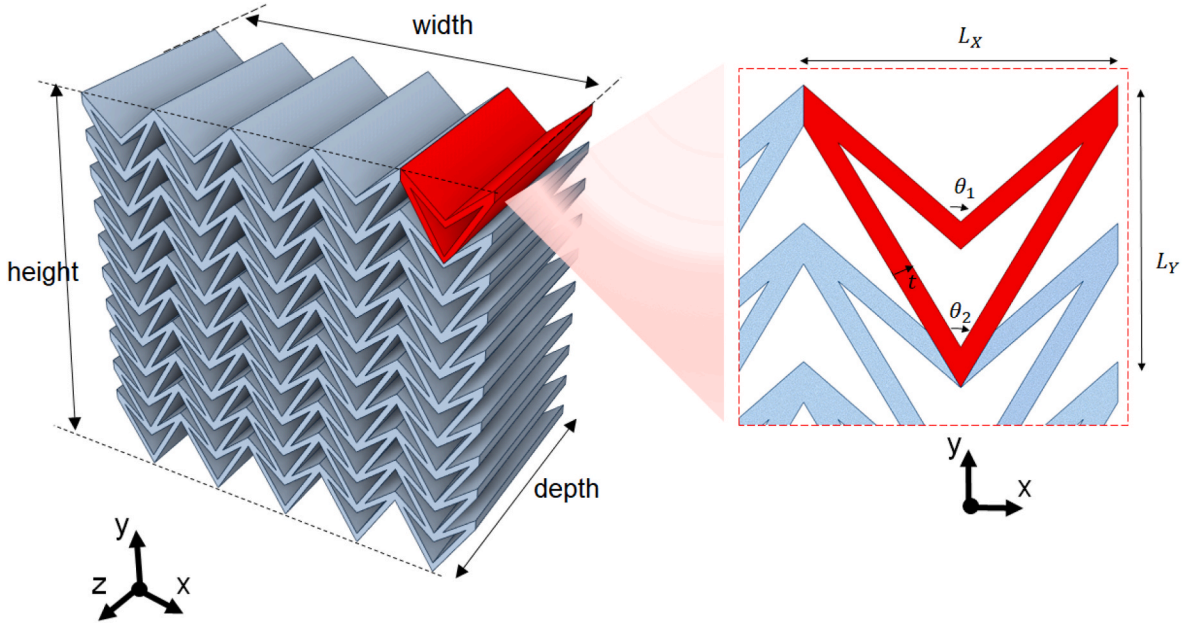

Fig. 2. Representation of 2D double arrow-headed lattice structure and its unit cell.

2.2. Manufacturing

2.2.1. Materials

Ti–6Al–4V (Ti64) spherical powder (Arcam AB, Sweden) with the size distribution of D10, D50, and D90 were 60.3, 82.3, 110.9 μm, respectively, were obtained through plasma atomization was used as the starting material. The particle size distributions (PSD) were measured using a Mastersizer 3000E (Malvern Panalytical, UK). The chemical composition of Arcam AB Ti64 powders used in this study is given in Table 1. These commercial Ti64 powders contain mostly no entrapped porosities or satellites, resulting in good flowability and packing density.

2.2.2. Electron beam powder bed fusion (PBF-EB)

ARCAM's PBF-EB system (Arcam Q10, Arcam AB, acquired by GE Additive) was used to print the samples. STL files were processed in Magic software and exported to the PBF-EB machine for manufacturing. The mass of the lattice blocks is 134 ± 3 g, with an 6 % deviation recorded compared to the designed mass of 142.6 g. This deviation is attributed to the build orientation and cleaning process of the attached powders. To reach a shortlist of process parameters, cubic samples with $1 \times 1x1\ cm^3$ were printed within a large parameter window. After visual checks of cubes, some selected parameter sets were employed to print unit cells of three type lattice structures. Then, three sets that were given in Table 2 were employed for the manufacturing of lattice blocks. A 0° build angle corresponds to an orientation where the x-z plane of lattice structures (as shown in Fig. 3-a) is parallel to the horizontal plane of the powder bed. Conversely, a 45° build angle represents an orientation where the x-z plane of DAH lattices is rotated 45° around the page's normal (z-axis), a rotation towards the vertical direction (height) of the powder bed. The scan speed function (SF) denotes a black box function, that was applied with a changing scan speed during the process by the machine's software. The other two sets with low speed (LS) and high-speed (HS) beam scans were used to build samples with the constraint of electron beam energy density of 24 J/mm^3. Within that constraint, the effects of different scan speeds and different build orientations (0° and 45°) were evaluated.

Table 1
Composition of the Ti–6Al–4V powder.

Element	Al	V	C	O	Fe	N	H	Ti
Weight [%]	6	4	0.03	0.15	0.1	0.01	0.003	Balance

2.3. Microstructural characterization

In order to predict the relation between the visually observed fracture locations at struts observed during the compression tests and microstructural features, microstructural characterizations were carried out focusing on the critical parts of unit cells. The investigated points were single thin wall and connection of multiple struts (thick strut) as details are given in the following sections.

2.3.1. Phase formation

Microstructural phase analysis of the unit-cell of Ti64 lattice structures was performed using X-ray diffraction (XRD, RINT-2500V, Rigaku, Japan) using Cu Kα radiation with a wavelength of 0.154 nm. The XRD data were obtained through point scanning in the 2Θ angular range from 30° to 80° for the lattice thin walls with a step size of 0.02° and a scan time of 2 s per step at room temperature. To identify the phases present, the signature spectra of the phases were indexed with diffraction patterns of the corresponding phase by using the X'Pert HighScore Plus software (PANalytical, Netherlands).

2.3.2. Porosity, density and thickness evaluations

The density at struts of the unit cell of Ti64 lattice structures were measured three times using the Archimedes' method (LA310S, 147 Sartorius, Germany). This measured density was calculated from the average absolute density of Ti64 (4.43 g/cm3) to confirm the comparable densification between process parameters and build orientations. The density of defects, such as porosity and/or lack of fusion, in Ti64 unit cells was observed in x-y and y-z cross sections (Fig. 3-b) and the defect percentage was determined by analyzing optical microscopy images (× 50 magnification) of the y-z cross section using the image analysis software ImageJ.

2.3.3. Surface morphology and microstructure evaluations using SEM-EBSD

Microstructural analyses of the Ti64 samples fabricated by PBF-EB with different scan speed and build orientations were conducted to clarify the possible effect of the microstructural characteristics on

Table 2
PBF-EB process parameters to fabricate lattice blocks.

Scan speed type	Sample code	Build orientation [°]	U [kV]	I [mA]	V [mm/s]	Line offset [mm]	Thickness [mm]	E [J/mm^3]	Focus offset [mA]
High-Speed (HS)	0deg-HS	0	60	20	10000	0.1	0.05	24	10
	45deg-HS	45							
Low-Speed (LS)	0deg-LS	0	60	5	2500	0.1	0.05	24	10
	45deg-LS	45							
Speed Function (SF)	0deg-SF	0	60	SF (−160)	SF (−160)	0.1	0.05	–	10
	45deg-SF	45							

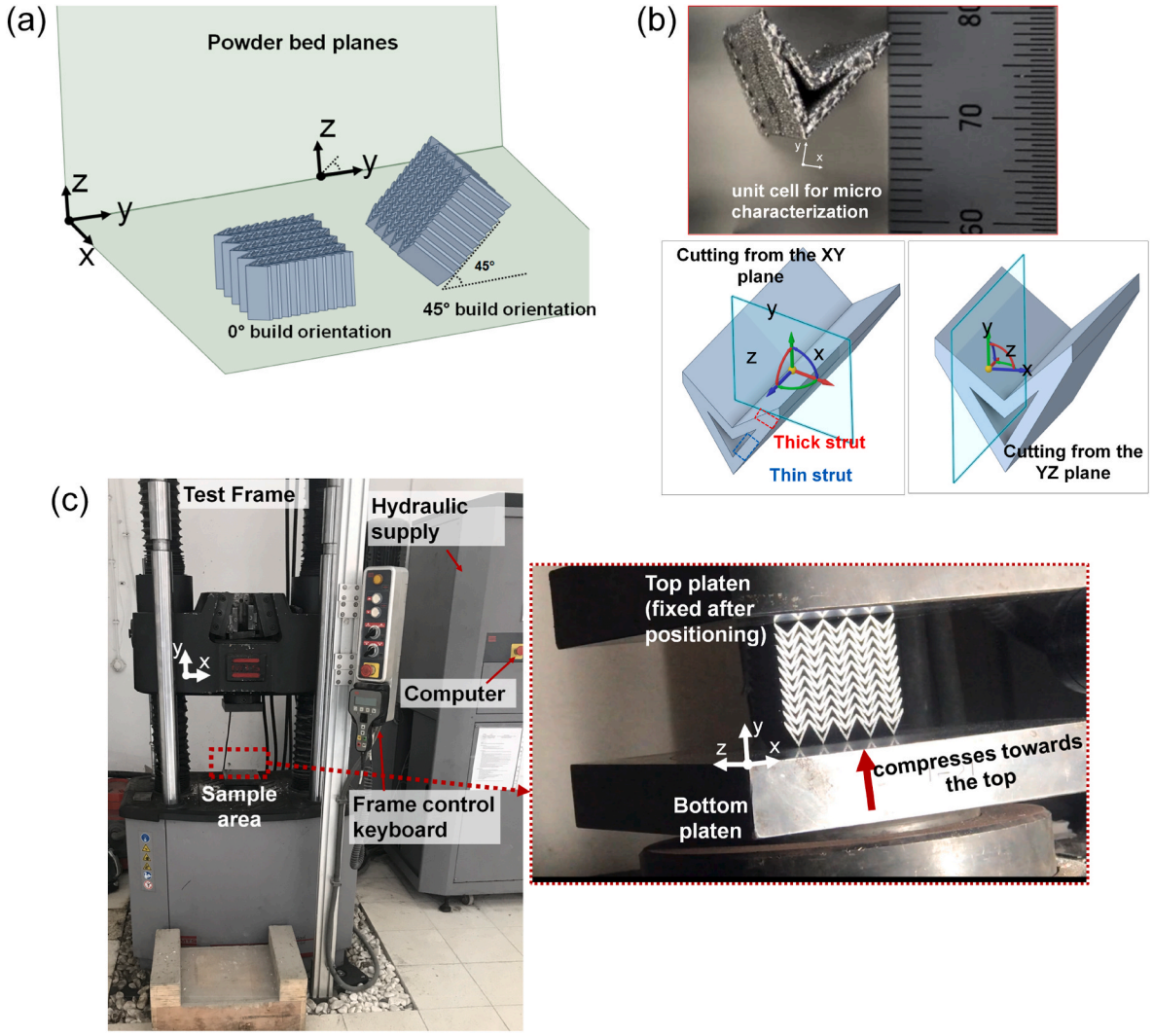

Fig. 3. (a) Powder bed build planes and orientations: 0° and 45°. (b) Example of produced unit-cell for micro-characterization with x-y and y-z cut planes. (c) Quasi-static compression test setup and a sample 2D lattice structure placed between platens.

energy absorption behavior under compression. The microstructural characterization was conducted on the x-y plane (perpendicular to build direction). The x-y cross section of the unit lattice was obtained by electrical discharge wire cutting. The cross sections were mirror-polished and observed using FE-SEM. The critical sections (thin wall and thick strut) of the lattice structures were observed by filed-emission scanning electron microscopy (FE-SEM; JEOL JIB-4610F, Japan) equipped with an electron backscatter diffraction system (EBSD, NordlysMax3 system, Oxford Instruments, UK, operated with a 20 kV accelerating voltage to clarify the microstructural features and the attached powders. Then, HKL Channel 5 software (Oxford Instruments, UK) was used to clean the non-indexed pixels and visualize the obtained EBSD data. From these results, the quantitative analysis of the average grain size, grain orientation ratios, and Kernel average misorientation (KAM) were measured.

2.4. Compression experiments

The MTS's a 600 kN capacity static-hydraulic universal test system (Criterion® Series 60, Model 64.605) was utilized in conducting compression tests on the lattice structures, with a constant compression rate of 5 mm/min. The lattice structure was placed between two platens of the test frame as shown in Fig. 3-c, with the top plate held in a fixed position while the bottom plate compressed the lattice structure. Table 3 provides information on the number and types of samples used for the compression tests. For safety reasons, the tests were automatically

Table 3
Compression test samples with information of PBF-EB process.

Build orientation [°]	Scan speed type	Sample code	Number of samples
0	High-Speed (HS)	0deg-HS	5
	Low-Speed (LS)	0deg-LS	3[a]
	Speed Function (SF)	0deg-SF	5
45	High-Speed (HS)	45deg-HS	5
	Low-Speed (LS)	45deg-LS	5
	Speed Function (SF)	45deg-SF	5

[a] Number of employed curves due to failed two attempts out of five tests.

terminated when the compression strain dropped by 95 %. The compression results were assessed in terms of absorbed energy and force-deflection curves.

2.5. Finite element analyses

After modeling 2D DAH lattice structures with dimensions of 50 mm × 45.1 mm x 25 mm in CAD software, they were exported to the ABAQUS environment to create finite element models for quasi-static compression analyses. The base material, Ti64, was modeled with a Young's modulus of 110 GPa, a density of 4430 kg/mm3, and a Poisson's ratio of 0.3. To simulate the post-elastic behavior, stress-strain data from tensile tests were utilized.

The tensile tests were conducted on the MTS's 100 kN capacity static-hydraulic universal test system (Model 322.21), and the force data from the system's sensor and nominal strain from processed images with DIC (Camera of Allied Vision, Germany) were used to create true stress-strain curves. Small size specimens were taken into account for tests due to the size of lattice blocks. The plane-stress type (thickness (t): 1 mm, a gauge length (GL): 5 mm) and round type specimens (diameter: 4.75 mm, GL: 15.66 mm) were tested. As an example, snapshots representing the initial state, before the failure, and the failed state were provided for plane stress-type samples in the Appendix. DIC proved to be effective in capturing the localized plastic yield at necking zones for such small-sized specimens. In turn, the obtained strain at critical subsets of the images showed that the failure strain was around 0.05 mm/mm (5 %). The yield strength in the tests was above 900 MPa which is consistent with the literature. The tensile tests in the literature covers different size samples and different PBF-EB parameters, and yield strength ranges between 783 and 1100 MPa [51–54]. Additionally, the absorbed energy curve of the 45deg-SF block was employed to calibrate the Johnson-Cook (JC) parameters (A, B, n) for the numerical verification. Then, JC strength model in Abaqus was employed. It is given as

$$\sigma = \left(A + B\varepsilon_P^n\right)(1 + c\ln\varepsilon^*)(1 - T^*) \tag{3}$$

where σ represents the von Mises equivalent flow stress, ε_P^n is the equivalent plastic strain, ε^* is the dimensionless plastic rate. T^* is the homologous temperature. c is the strain rate sensitivity coefficient and can be employed as 0.029 from Ref. [54]. However, it only becomes effective at high strain rates. The parameters are summarized in Table 4. eq. (3) plots a plastic flow curve without stating the failure point. Therefore, a damage behavior is utilized to degrade the material, finally fail it. For this behavior, the Johnson-Cook damage model is introduced through D_1 (initial failure strain), D_2 (exponential factor), D_3 (triaxiality factor) damage material parameters in Abaqus Explicit Solver [55]. D_4 (strain-rate factor) and D_5 (temperature factor) were not used due to quasi-static and room temperature conditions. The damage model is expressed as

$$\varepsilon_f = \left[D_1 + D_2\, exp\left(D_3\left(\frac{\sigma_m}{\sigma_{eq}}\right)\right)\right] + \left[1 + D_4\ln\left(\dot{\varepsilon}_p^*\right)\right][1 + D_5 T^*] \tag{4}$$

$$D = \sum\left(\frac{\Delta\varepsilon}{\varepsilon_f}\right) \tag{5}$$

$$\sigma_D = (1 - D)\sigma_{eq} \tag{6}$$

where σ_m, σ_{eq} and σ_D are mean, equivalent and damage stresses, respectively. ε_f is a statement based on stress triaxiality $\frac{\sigma_m}{\sigma_{eq}}$, strain rate $\dot{\varepsilon}_p^*$ and temperature T^*. D_1, D_2, D_3 and G_C are listed in Table 4. The various studies in the literature have used comparable values for D_1- D_4 [53,56]. The compression modes in the experiments which are discussed later in the results section, were also considered to achieve a similar collapse progression in the numerical simulations. To accomplish this, after reaching to the maximum degradation, elements removal was activated due to sharp edges and multiple collapse zones. Additionally, weaker interconnection zones were identified in the experimental observations during compression tests, and modified JC plasticity parameters were introduced for those.

Fig. 4 shows the assembly, weaker interconnection zones, and representative mesh model of the DAH lattice block. Roughly 1.5 M of C3D10M type elements were employed. As the explicit solver was employed [57], appropriate artificial mass scaling was utilized to accelerate analyses within the constraint of maximum 10 % kinetic energy of total internal energy. The weak zones in Fig. 4-b were utilized owing to outcomes from the experimental compression patterns which are later given in the results section.

3. Results and discussion

3.1. Microstructural characterizations

3.1.1. Phase formation

Fig. 5 presents the XRD patterns of the single struts along its build direction (y-z plane in Fig. 3-b) in the unit-cell of Ti64 DAH lattice structures fabricated with different process parameters. In all XRD patterns, hcp α peaks were observed as the main phase which are related to α and α' phases. While the remaining prior β phase was detected as a minor phase, there were no other peaks from bcc β phase, indicating that the fraction of the β phase is considerably low in as-built unit-cells. In the literature, it has been reported that thin wall (≤1 mm) sections exhibited a mixed microstructure of α/β and martensite α' plates [58], which correlates with the phase formation according to the XRD results.

3.1.2. Porosity, density and thickness evaluations

Fig. 6 shows optical microscope images of 0° built DAH unit cells at x-y and y-z planes fabricated with different PBF-EB process parameters. The images highlight that different scan speeds within same energy density of 24 J/mm^3 and with automatic speed function did not affect the characteristics of defects consisted of irregular shape lack of fusion and spherical pores. The structural integrity of DAH unit cells (Fig. 6-a) was not differed with the change of process parameters. However, the percentage of the porosity increased with increasing scan speed (Fig. 6-b), which was 0.12 % for 0deg-LS and increased to 0.17 % and 0.18 % for 0deg-HS and 0deg-SF, respectively. Automatic scan speed function is expected to optimize the applied beam energy according to the scan

Table 4
Johnson-Cook plasticity and damage model parameters for Ti64, respectively.

A [MPa]	B [MPa]	n	C ref. [44]	m	Strain rate [1/s]	D1	D2	D3	G_C [MPa $\sqrt{m}$]
870-950[a]	450-550[a]	0.34	0.029	0.8	1	0.05	0.27	−0.48	49.9–100

[a] As DAH block samples of SF, HS, and LS can absorb different energies, parameters slightly differ in the numerical calibration.

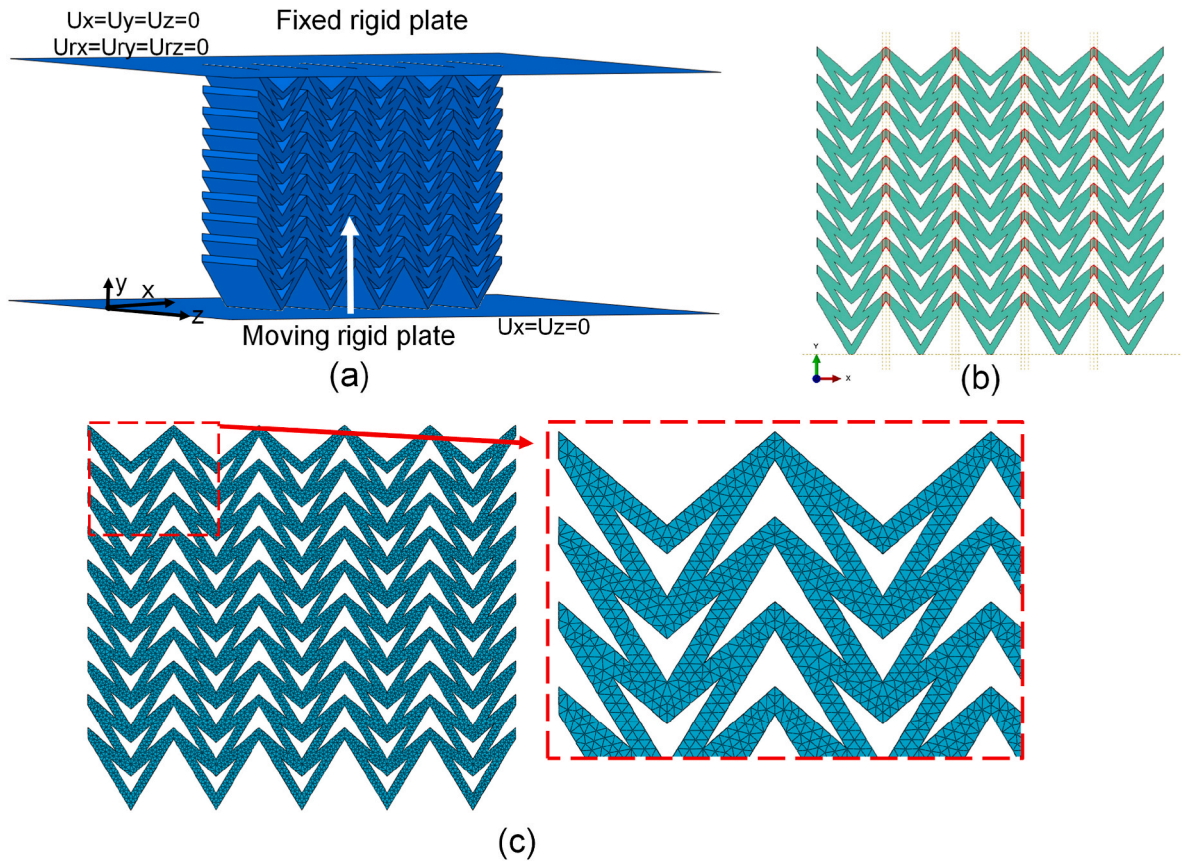

Fig. 4. (a) Assembly model of lattice block, rigid fixed plate and moving rigid compression plate. (b) The DAH lattice block with weak interconnection sections between columns. (c) Mesh model of the lattice block with tetrahedral elements.

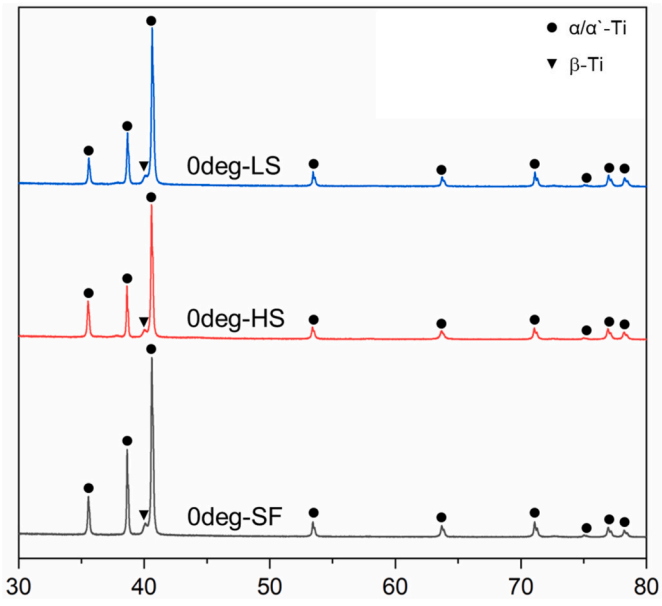

Fig. 5. X-ray diffraction patterns in unit-cells of Ti64 DAH lattice structures fabricated with different process parameters by PBF-EB.

length with the control of scan speed [59].

Measured density through Archimedes test as shown in Fig. 7 exhibited same tendency with the porosity measurements (Fig. 6). The porosity increased with the decreasing scan speed, thus, measured density at struts of 0deg-LS and 45deg-LS unit cells reached the highest comparing to the ones with the same build orientation. It is important to note that the unit-cells with 0° build orientation showed higher density than 45° samples. This difference was attributed to the support design. As reported previously, the addition and design of the support structure could change the cooling rates, resulting differences in microstructure and densification [60].

Fig. 8 shows measured strut thicknesses of 0° and 45° built DAH unit cell samples with different process parameters. Seven measurements were made on each image to reach an average thickness of the struts. These average values are within ±4% of 0.8 mm although a few locations gave beyond the average range due to the instability of melt pool forming liquid droplets and/or un-melted attached powders. Note that 0.8 mm strut thickness in CAD, measured thicknesses were coherent to the design. Yet, a slight difference due to the process parameters was also seen, in which struts built as 0° and 45° with low speed scan (0deg-LS and 45deg-LS) had lower thicknesses of 0.02 and 0.03 mm comparing to high scan speed ones (0deg-HS and 45deg-HS), respectively.

3.1.3. Surface morphology and microstructure evaluations using SEM-EBSD

Fig. 9-a presents that, failures/damage initiated at thin strut regions rather than thick strut region at compression tests (red dots representing failed points on the struts). One reason is based on the geometry, and the stress concentrates at thin regions of the unit cells. Then, failures initiated as expected due to less strength at these thin cross sections. Another reason is high residual stress deployed at thin struts. According to the EBSD analysis, it is understood that thin and thick strut regions differed regarding the residual stress identified with KAM, as expected due to the difference in scan length or can be considered as the difference in wall thickness [61,62]. Although 0° and 45° DAH lattices fabricated with different thermal history, the tendency of higher residual stress at thin

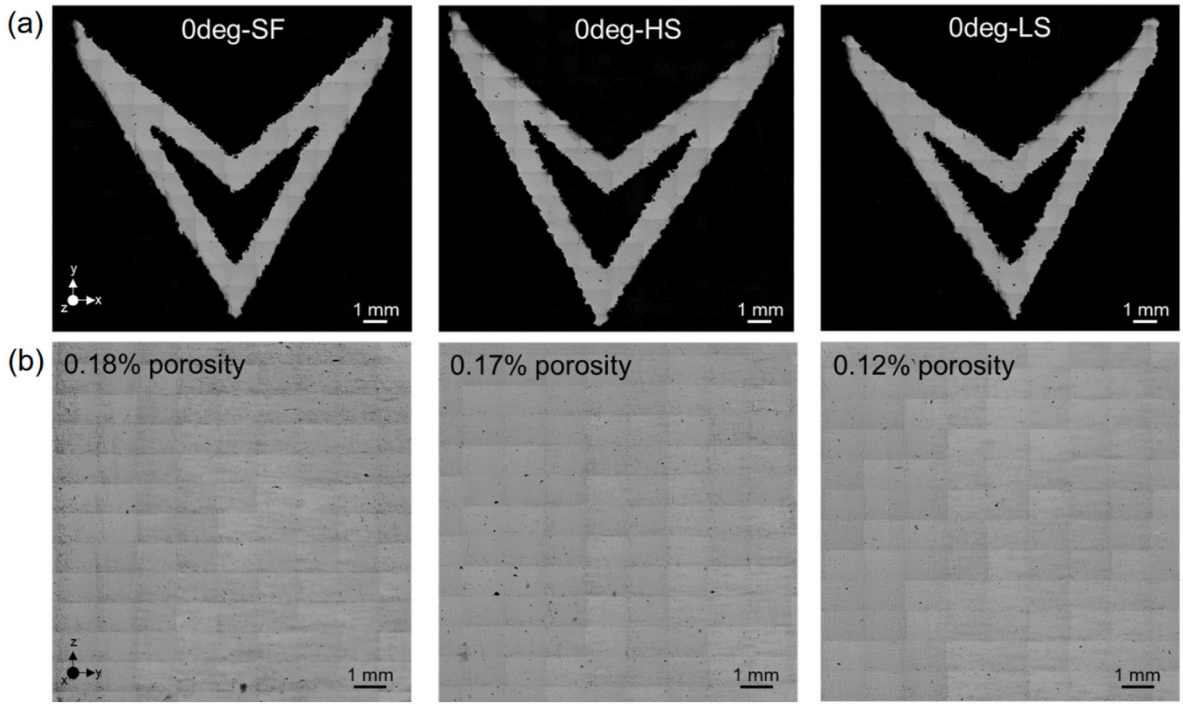

Fig. 6. Optical microscope images of 0° samples with 3-different scan speeds observed on (a) x-y plane and (b) y-z plane.

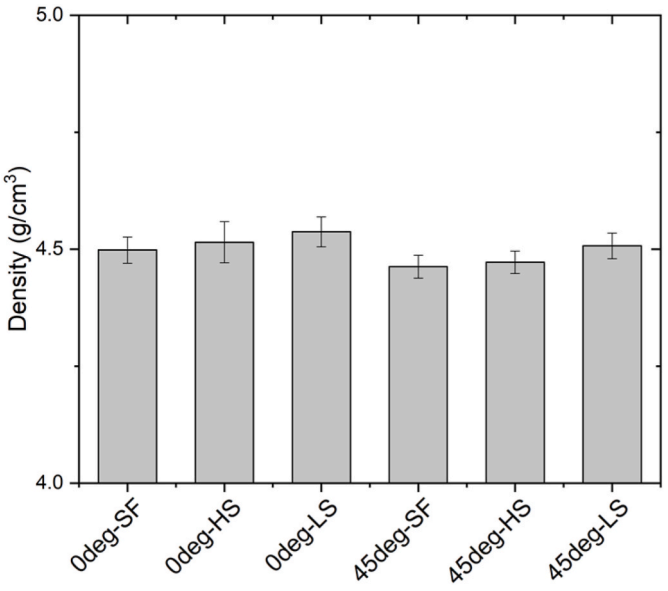

Fig. 7. Relative density of samples fabricated with different speeds and build direction.

strut and the thick region was the same, however, the KAM values was lower in the case of 45° DAH lattice (0deg-SF; thick strut: 1.20, thin strut: 1.06.45deg-SF; thick strut: 1.15, thin strut: 1.01 in Fig. 9-c and -d) expected to be the reason of the build height, which resulted longer heat exposure, thus, decreasing the thermal stress overall. On the other hand, there was no nortworthy difference in texture formation or phase distribution acording to IPF map and phase map, respectively.

0° and 45° DAH lattices fabricated with the same process parameters showed no significant differences in the microstructural features other than KAM values (Fig. 9-c and -d). Therefore, the microstructure of 0° DAH lattices fabricated with different process parameters were investigated considering phase structure (phase map of α/α' and β), texture (IPF), and residual stress distribution (KAM) of thin and thick struts as shown in Fig. 10. SEM images exhibited thin and thick strut regions of 0° DAH lattices with sintered powders attached to the strut during preheating and melting, causing rough surface quality. The detail microstructural analysis was carried out at the locations indicated as square areas with the number of 1 and 2 on the SEM images, indicating thin wall and thick strut, respectively. In general, the results were consisted with findings presented in Fig. 9, showing mainly α/α' lath formation with no distinctive texture formation or grain size differences (1.35 ± 0.05 μm). However, the tendency of higher accumulated stress on thin strut areas was the same for each process parameter, although applied speed function process parameter decreased the difference in residual stress between thin and thick struts, resulting 0.97 KAM value for both, owing to its close-packed program aiming to optimize thermal distribution in each build layer. While the KAM of thick struts for 0deg-HS and 0deg-LS were 0.81 and 0.88, respectively, thin struts accumulated higher stress due to faster cooling rate with shorter scan length and less scan area, thus showed higher KAM value, reaching 0.98 and 1.00 for 0deg-HS and 0deg-LS, respectively.

3.2. Compression results

Fig. 11 summarizes the compression deformation of DAH lattice structures built in the 0° and 45° orientations under a constant compression rate of 5 mm/min. Note that for each of the two built directions, three different scan speeds were employed. During the quasi-static tests, the general deformation patterns can be summarized as follows:

- Firstly, there was a short phase of elastic compression, exhibiting a negative Poisson's ratio, followed by initiation of the local buckling at the bottom cells (deformed thin struts), as highlighted in the second column.
- Then, separations started to occur between cells, with the weakest regions being the connections between columns (or between cells), as shown in the third column. Additionally, a few lines of cells had already collapsed at that time.

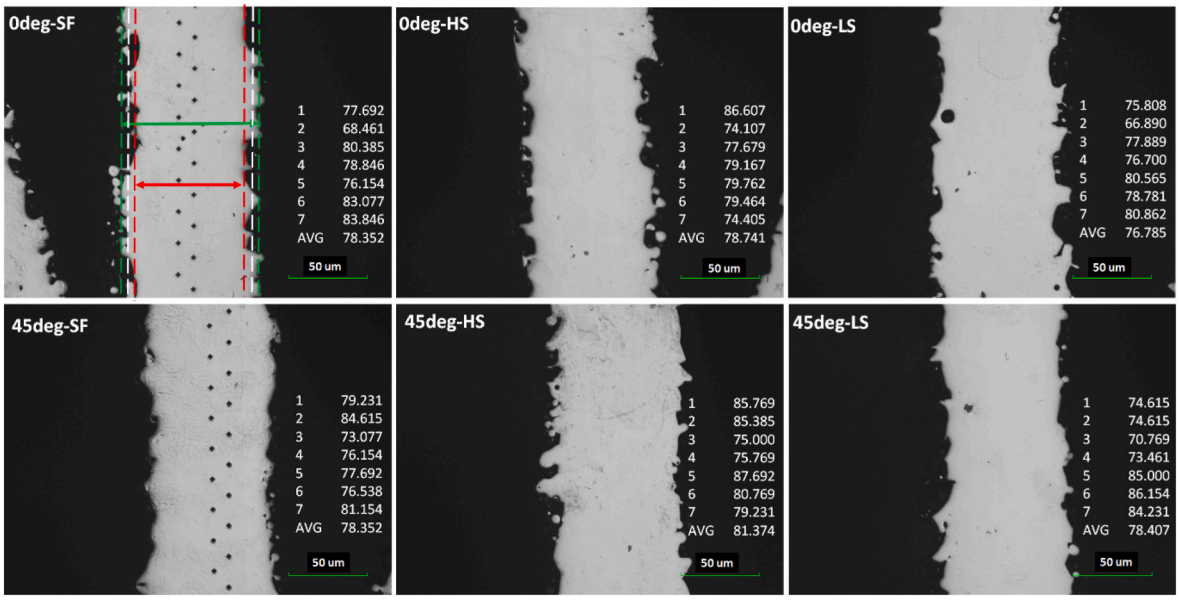

Fig. 8. Optical microscope images for the strut thicknesses, and 7- measurements from different locations.

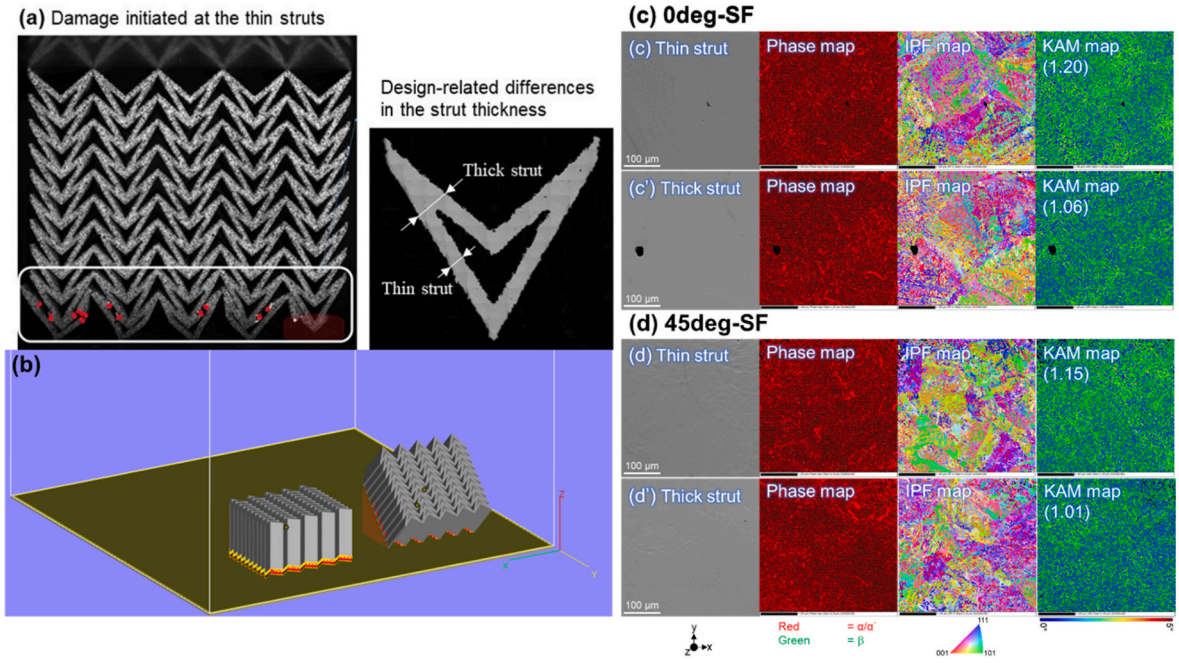

Fig. 9. (a) The representation of initiation of failures at "thin strut" locations of the bottom of the blocks during the compression test. (b) 0° and 45° DAH lattice structures with the support structure design on Magics software. And detail investigation of "thin strut" and "thick strut" of 0° (c) and 45° (d) DAH lattices regarding phase maps, IPF maps, and KAM maps.

- Next, a continuous line of failure separations between columns from bottom to top became apparent, as given in the fourth column. It was also observed that during the motion of the platen, some pieces of several samples separated without collapsing due to sudden fracture and did not contribute to the force-deformation responses.

  Additionally, key outcomes of the observations were listed below:

- Based on the patterns shown in the third column, if the connections between the columns were stronger, some of the columns did not lean towards the sides. This would allow the block to exhibit a longer period of elastic compression with a negative Poisson's ratio and local plastic buckling, which in turn could increase the energy absorption.
- Based on the patterns shown in the second to fourth columns, the main patterns in all tests were similar, with local collapse zones similarly populated below and columns starting to separate, limiting the energy absorption through local buckling.
- Although the overall trend was similar, close inspection of repeated tests of the same type of blocks showed that fracture initiation and progression of failures occurred at dissimilar locations due to the strong anisotropy and inner imperfections arising from the additive manufacturing technique.

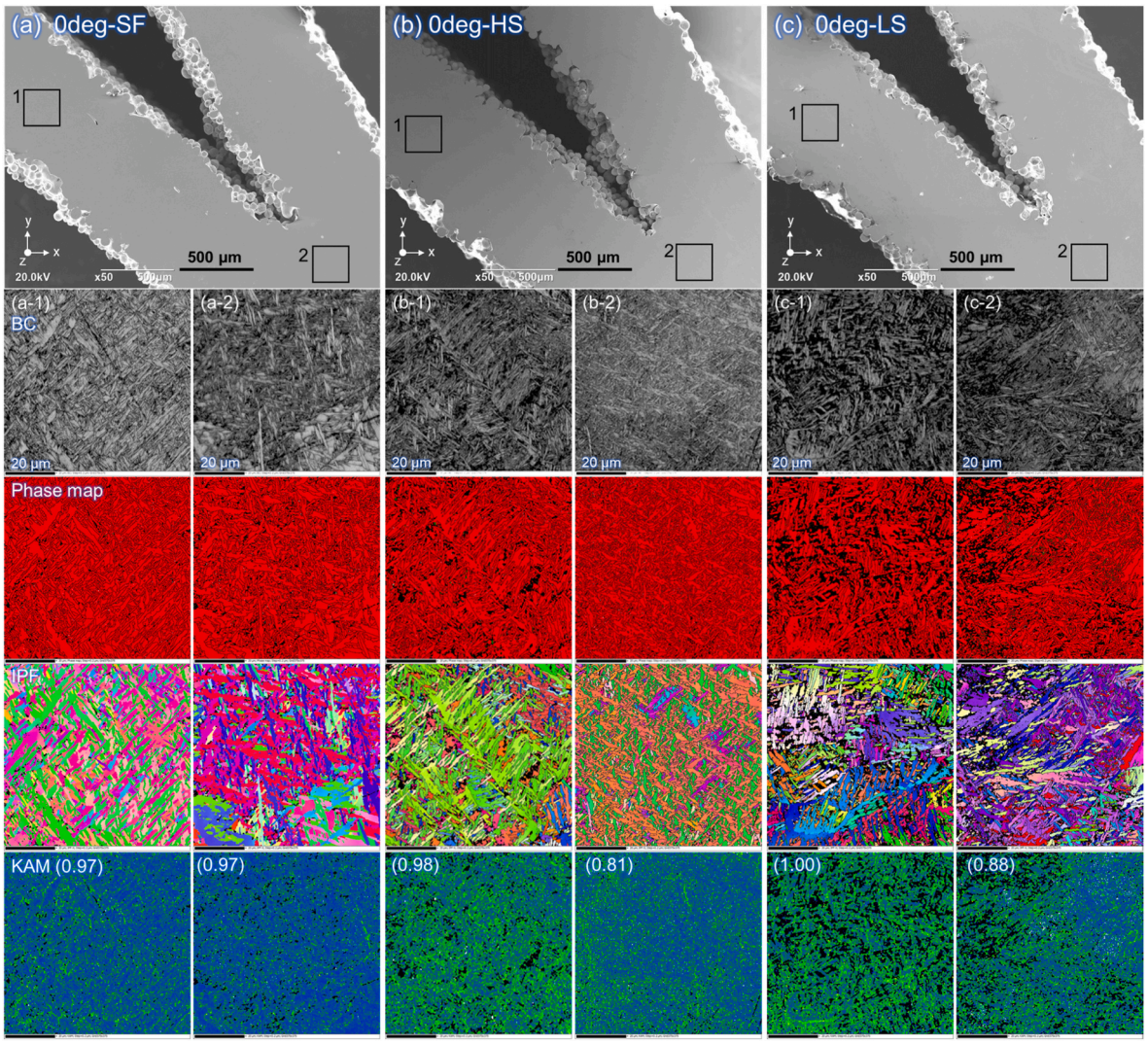

Fig. 10. SEM images of thin and thick strut regions of 0° DAH lattices fabricated with different process parameters (a–c). EBSD analysis of thin and thick strut regions to identify phase distribution, texture formation, and residual stress accumulation.

- For the samples built with different scan speeds, it is not possible to make an apparent classification based on the visual deformation modes. However, one of the factors affecting the deformation modes was previously mentioned regarding microstructural features of 0° and 45° built samples in Fig. 10, which is the stress localization at thin struts indicated by higher KAM values. Thus, the early stage deformation was observed at the thin struts of bottom cells.
- For the samples built in different orientations (0° and 45°) different level residual stresses, did not cause a specific collapse pattern due to many other sources such as micro-porosities and strut wall anomalies.

Although all samples exhibited similar main crushing modes, the collapse shapes differed due to the initiation and development of failures at different struts, strongly affecting the force curves. Fig. 12 shows reaction forces-deflection curves. It is apparent that the initial reaction force peaks are coherent each other (Note: The initial peaks were intended to be higher when initial fractures did not happen at a few struts). And new peaks occurred after a group of row collapsed. As the collapses continued to next step, the level of peak curves started to differ to each other due to differences in the number of locations of failures, as shown in the deformation snapshots in Fig. 11.

The averages of peak reaction forces were listed in Table 5, and a summary is given below:

- While 0deg-SF group exhibited peak reaction forces of 127.62 ± std 11.98 kN, 45deg-SF group exhibited 138.00 ± std 14.60 kN. Namely, 45deg-SFs exhibited 8.1 % higher peak than 0deg-SFs.
- 0deg-LS group and 45deg-LS group exhibited peak reaction forces of 143.100 ± std 7.11 kN and 143.84 ± std 7.02 kN respectively. Both exhibited similar average peaks. These samples exhibited the largest peak reaction forces among all test sets, as well as low standard deviations.
- 0deg-HS group and 45deg-HS group exhibited peak reaction forces of 121.38 ± std 12.65 kN, and 139.47 ± std 13.32 kN, respectively. 45deg-HS blocks exhibited 15 % higher peak reaction forces than of 0deg-HS group. Additionally, 0deg-HS group exhibited the largest standard deviation among all test sets.

Overall, 45deg samples had slightly less standard deviations comparing to their 0deg counterparts. 0deg-LS group exhibited 12.8 % and 18.6 % higher average peak forces than 0deg-SF and 0deg-HS groups, respectively. 45deg-LS group exhibited 4.2 % and 3.14 % higher average peak forces than 45deg-SF and 45deg-HS groups, respectively. It is explicitly seen that manufacturing samples at 45°, took HS and SF groups closer to the peaks of LS samples It is important to note

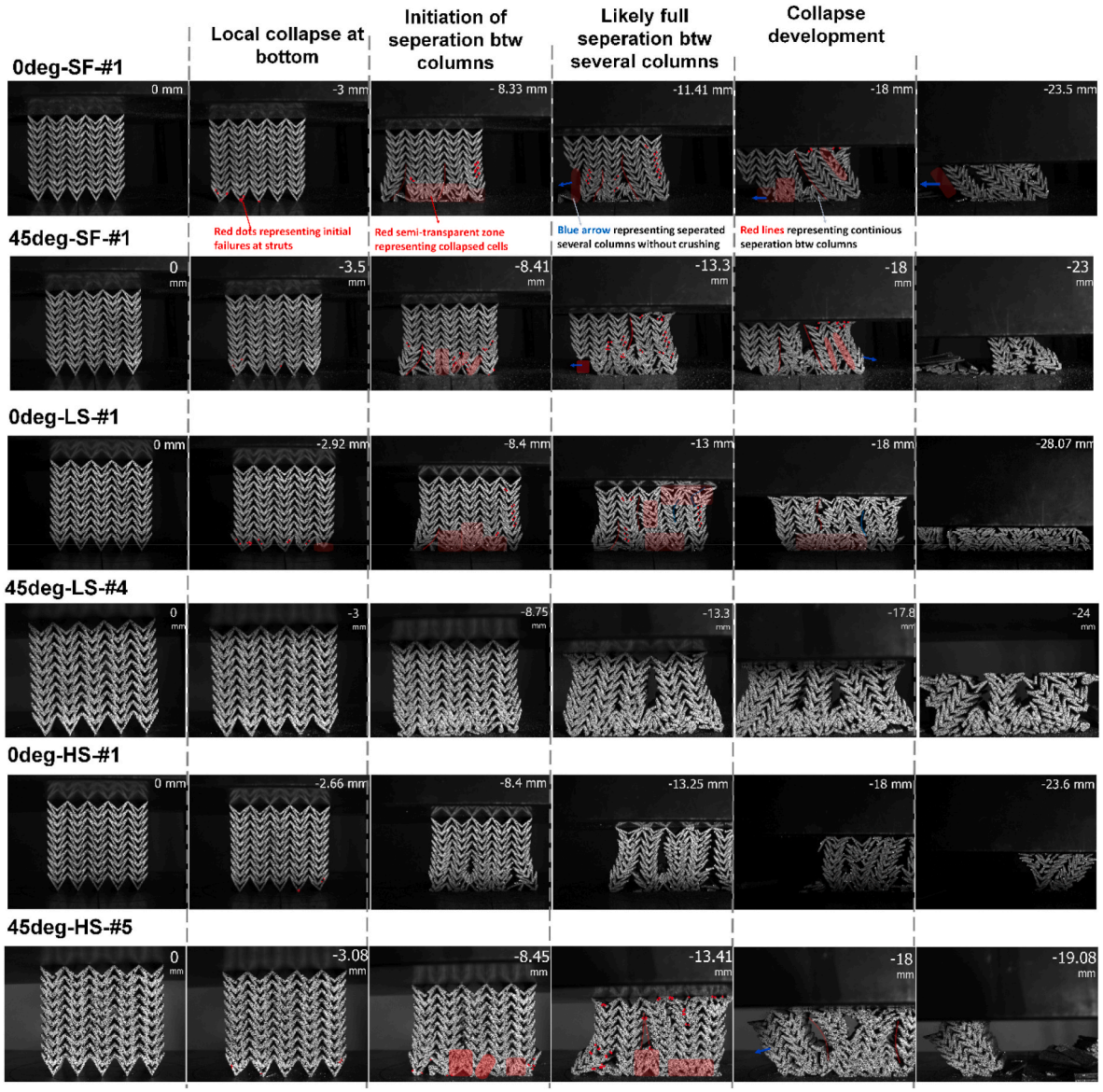

Fig. 11. Snapshots at certain times during compressions of double arrow headed lattice structures. Each row represents a sample from 5 repeated tests of each type. The rows are DAH 0deg-SF #1, 45deg-SF #1, 0deg-LS #1, 45deg-LS #4, 0deg-HS #1, 45deg-HS #5, respectively (red dots: local and initial failure points, red clouds: compressed zones, arrows: Indication of fall directions of columns.).

that KAM values revealed that unit cell samples built with low scan speed exhibited low residual stress. Additionally, these had the lowest micro-porosities, where this could contribute to have a low standard deviation as well. In general, DAH lattice structures exhibited many peaks in similar levels. As imperfections could affect the stiffness during the compression, the peaks of reaction forces could differ due to level or position of the imperfections. After separation/fracture at each row, next peaks triggered.

Table 6 lists absorbed energies at 10 mm and 15 mm, respectively. Fig. 13 highlights absorbed energies grouped for samples built at 0° and 45° as the scan speed of beam created significant variance among low-speed and high-speed scans. For absorbed energies at 10 mm, 0deg-SF and 45deg-SF groups dissipated 0.743 kJ and 0.744 kJ, respectively. 0deg-LS and 45deg-LS groups dissipated 0.833 kJ and 0.801 kJ, respectively. 0deg-HS and 45deg-HS groups dissipated 0.725 and 0.765 kJ, respectively. Specifically, 0° samples built with low scan speed absorbed 12 % and 14.9 % higher energy than samples built with speed function scan and high scan speed, respectively. 45° samples built with low scan speed absorbed 7.7 % and 4.7 % higher energy than samples built with speed function and high scan speed, respectively. For each scan type, 45° samples had less standard deviation than those built at 0°. For absorbed energies at 15 mm, standard deviations in absorption levels increased compared to the levels at 10 mm. However, samples built at 45° still had less deviations than those built at 0° (except LS samples). 0deg-SF and 45deg-SF groups dissipated 1.020 kJ and 1.128 kJ, respectively. 0deg-LS and 45deg-LS groups dissipated 1.241 kJ and 1.188 kJ, respectively. 0deg-HS and 45deg-HS groups dissipated 1.001 kJ and 1.155 kJ, respectively. Specifically, samples built at 0° with low scan speed absorbed 21.6 % and 24 % more energy than samples built with scan speed function and high scan speed, respectively. Samples built at 45° with low scan speed absorbed 5.3 % and 2.9 % more energy than samples built with scan speed function and high scan speed, respectively. It is clearly seen that the effect of scan speed was captured strongly at 0° samples while this effect was not as pronounced for 45° samples at 15 mm. For absorbed energies at 20 mm, deviations in absorption levels become more obvious as some of pieces separated from the sample without compression, as shown in the last two columns of Fig. 11.

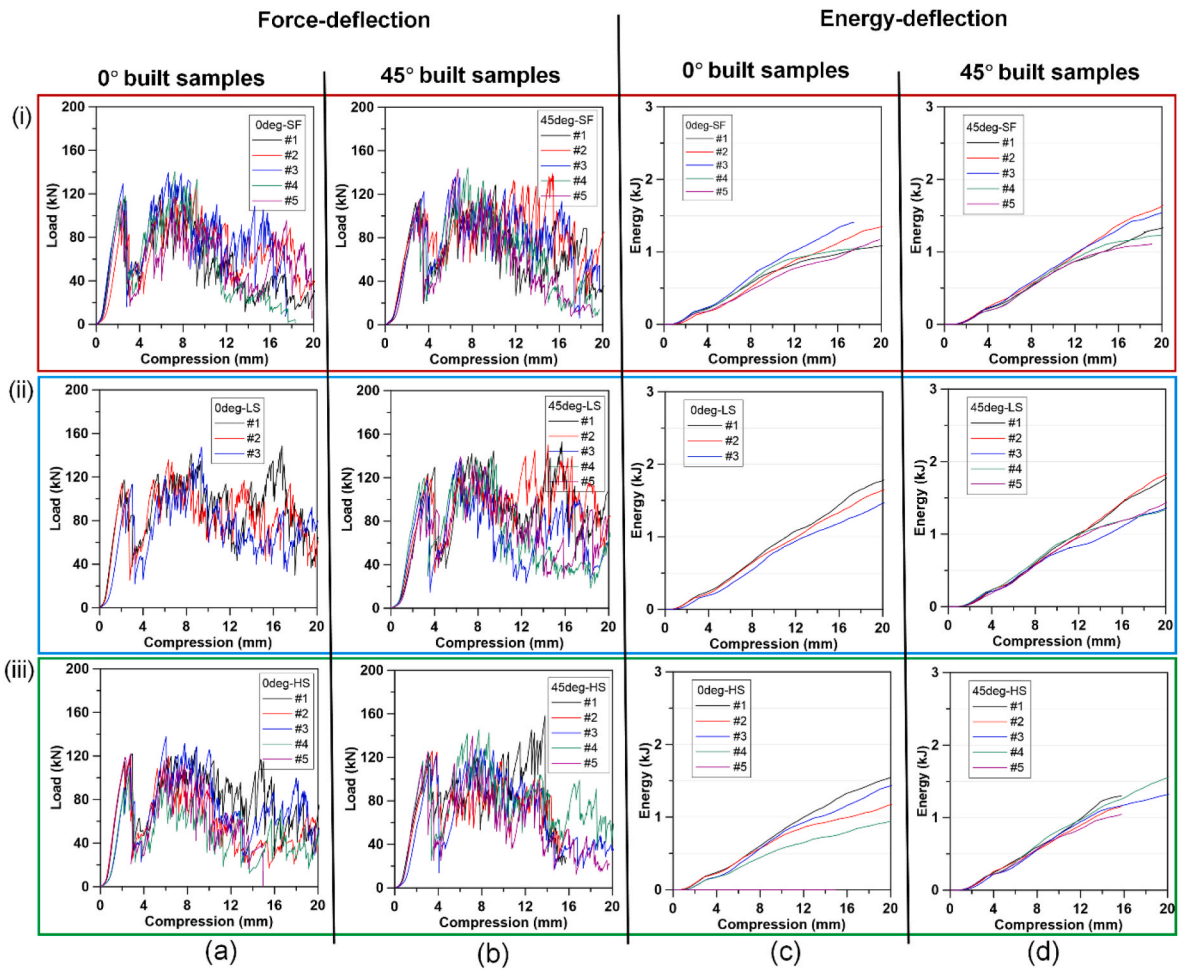

Fig. 12. DAH lattice blocks built by three different beam scan speeds. Reaction force-deflection curves of (a) **0**° built (0deg-SF, 0deg-LS, 0deg-HS) and (b) **45**° built (45deg-SF, 45deg-LS, 45deg-HS) samples. Absorbed energy deflection curves of (c) **0**° built, and (d) **45**° built samples, respectively.

Table 5
Peak reaction forces recorded in quasi-static compression tests.

	0deg-SF	45deg-SF	0deg-HS	45deg-HS	0deg-LS	45deg-LS
Avg [kN]	127.62	138.00	121.38	139.47	143.90	143.84
Std [kN]	11.98	6.40	12.65	13.32	7.11	7.02
Std [%]	9.39	4.64	10.42	9.55	4.94	4.88

3.3. Finite element analyses

The outcomes from the compression tests such as energy absorption-deflection curves, compression patterns, weak zones at the manufactured samples were used to create more realistic numerical models. Therefore, without these results, it is not possible to have accurate patterns. The parameters in the Johnson-Cook strength model (A, B, n) and damage model (D1, D2) were calibrated based on the observations in the experiments. In this manner, compression experiments hold a crucial role to calibrate numerical analyses. A parametric study such as in following section can be conducted based on these verified numerical models.

The compression tests produced a consistent collapse shape regardless of the different manufacturing parameters (such as built at 0° or 45° directions or varied scan speed under constant energy density). It can be reminded that as a representative of the collapse of DAH block, collapse pattern of 45deg-SF sample was used to validate the finite element re-

Table 6
Absorbed energies of DAH lattice blocks built with three different speeds recorded in quasi-static compression tests at 10, 15 and 20 mm, respectively (grouped per beam scan speed).

	at 10 mm (22 % compression)					
	0deg-SF	**45deg-SF**	**0deg-HS**	**45deg-HS**	**0deg-LS**	**45deg-LS**
Avg [kJ]	0.743	0.744	0.725	0.765	0.833	0.801
Std [kJ]	0.083	0.027	0.094	0.038	0.053	0.046
Std [%]	11.12	3.59	12.98	4.91	6.38	5.78
	at 15 mm (33 % compression)					
	0deg-SF	**45deg-SF**	**0deg-HS**	**45deg-HS**	**0deg-LS**	**45deg-LS**
Avg [kJ]	1.020	1.128	1.001	1.155	1.241	1.256
Std [kJ]	0.133	0.114	0.185	0.100	0.101	0.126
Std [%]	13.07	10.07	18.45	8.69	8.11	10.60
	at 20 mm (44 % compression)					
	0deg-SF	**45deg-SF**	**0deg-HS**	**45deg-HS**	**0deg-LS**	**45deg-LS**
Avg [kJ]	1.231	1.369	1.273	1.347	1.630	1.544
Std [kJ]	0.188	0.213	0.270	0.192	0.153	0.234
Std [%]	15.26	15.54	21.24	14.25	9.41	15.17

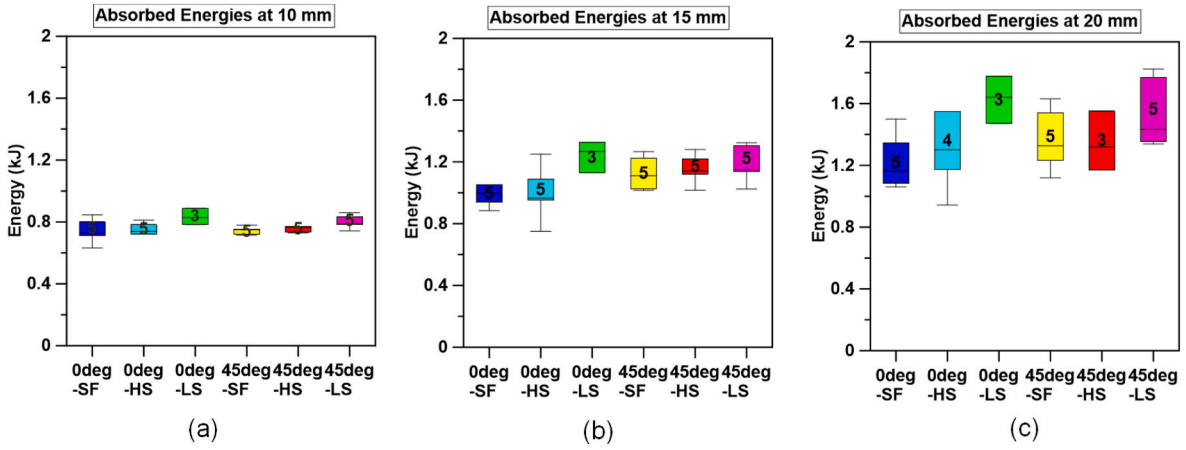

Fig. 13. Absorbed energies of DAH lattice blocks built by three different beam scan speeds at (a) 10 (22 %), (b) 15 (33 %), and (c) 20 (44 %) mm, respectively (grouped per built angles).

sults by comparing the peak forces and absorbed energies at specific times. During the experiments, the collapses originated from imperfect locations at the bottom. When a few rows at the bottom collapsed, the force curve peaked and then went to zero. As the columns separated from the bottom and moved towards the sides, the compression progressed based on these initial failures. Therefore, imperfections were introduced at the bottom lines. Fig. 14 shows energy-deflection curves of experiments and numerical analyses. At deflection of 15 mm (strain of 33 %), numerical analysis accurately predicted energy absorption with 1.1 kJ while DAH-45deg-SF samples exhibited absorption between 1.01 and 1.26 kJ in the experiments (while mass: 142.6 g, SEA: 7.08–8.83 kJ/kg). Fig. 15 shows collapse modes recorded in numerical analyses at different moments. Snapshots at 3 mm and 8.75 mm showed similar shapes such as a collapse at bottom couple of rows. Later, experimental modes of separation distinctly showed that imperfections between columns accelerated the separation between columns, and several columns lay down the sides without a compression.

Based on the compression modes obtained in the tests, the connection zones between unit cells in the vertical direction were modified as weaker sections, as shown in Fig. 4-b, because initial numerical trials failed to present separation between columns in the tests. This was attributed to weak bonding between the columns, which requires further considerations. The introducing the weak interconnection zones into the numerical models and calibrating damage behavior revealed that initially experimental observations are crucial in obtaining realistic compression models for the parts, built in the powder bed process. Then, this manufactured informed modeling can be followed in the parametric studies to enhance the performance by manipulating dimensional parameters.

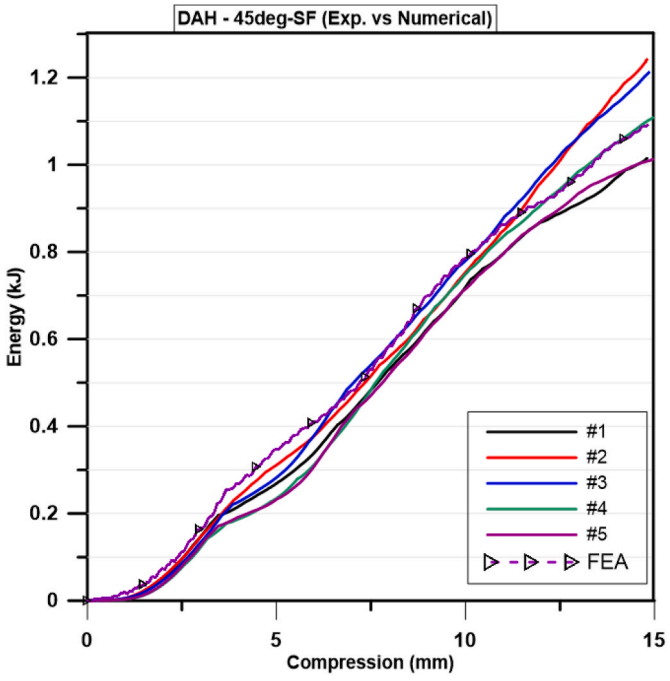

Fig. 14. Comparison of experimental (DAH-45deg-SF) and numerical modes during the quasi-static compression with 5 mm/min.

3.4. Parametric optimization

The compression results can be evaluated based on specific energy absorption (SEA), mean crush force (MCF), or crush force efficiency. When acceleration is not an important indicator for the design, achieving high specific energy absorption (SEA) is the main objective for an impact energy-absorbing mechanism. Before formulating a parametric problem, these variables are defined by the formulas given in eqs. (7)–(9).

$$EA = \int_0^{\delta} P(s)ds \tag{7}$$

$$SEA = \frac{EA}{m} \tag{8}$$

$$MCF = \frac{EA}{\delta} = \frac{\int_0^{\delta} P(s)ds}{\delta} \tag{9}$$

in addition to providing high impact energy absorption, the cellular design is also targeted to have a large gap volume in the block when used as a fluid flow channel. This study considers a multi-objective optimization problem by selecting certain weight fractions of the objectives to obtain high SEA (for the 50 % compression of the design) and low relative volume. The relative volume is calculated by dividing the total volume of the lattice structure's struts by the volume of the outline box containing the lattice structure. The problem is formulated as follows:

Maximize

$$F_1 = (w_{unit}, \theta_1, \theta_2, t) \cap F_2 = (w_{unit}, \theta_1, \theta_2, t)$$

Subject to

$10 \leq$ width of unit cell (w_{unit}) ≤ 16.6

$100 \leq$ outer angle (θ_1) ≤ 150

$50 \leq$ inner angle (θ_2) ≤ 90

$0.6 \leq$ thickness (t) ≤ 1.2

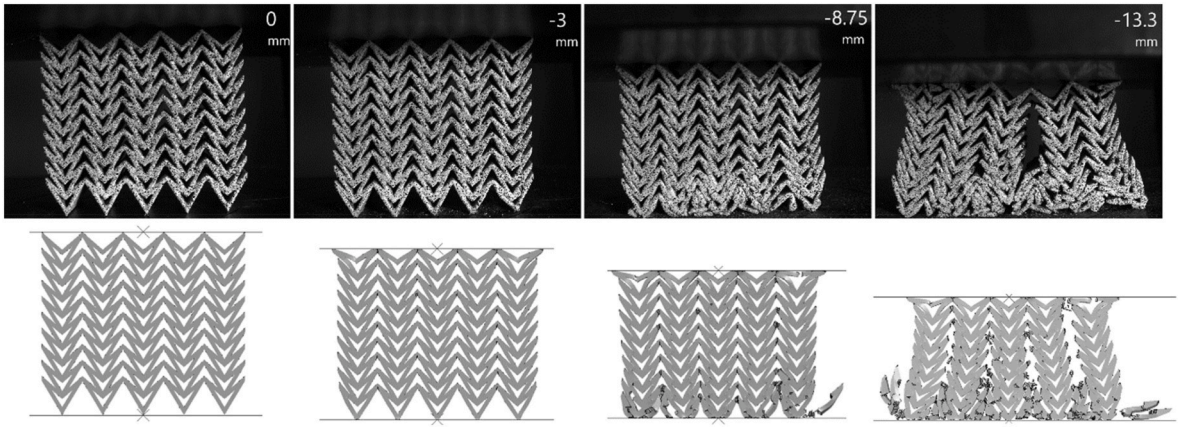

Fig. 15. Comparison of (a) experimental (DAH-45deg-SF), and (b) numerical modes during the quasi-static compression of a DAH block with 5 mm/min.

and number of columns ≤ 5, width <56 mm, depth = 25 mm

To create a design of experiments (DOE) for the four variables listed in Table 7, a three-level full factorial approach was used, which yielded 81 possible combinations (3^k). However, due to the time-consuming nature of numerical analyses, a subset of these combinations was created using a D-optimality criterion, resulting in a smaller DOE table with only 15 combinations, as shown in Table 8. Based on the design flow in the optimization problem, number of rows of the blocks were chosen equal to number of columns which is constrained in the problem. Therefore, height of each design could vary in a large range. Fig. 16 represents front views of each design in DOE. Finite element (FE) analyses were then performed for each of these 15 combinations.

To approximate the response, the response surface method (RSM) was employed. The quadratic polynomial model was fitted to the data in the DOE table. This approach enabled us to obtain an accurate representation of the response surface while minimizing the number of FE analyses required:

$$f = c_0 + \sum_{i=1}^{n} c_i x_i + \sum_{i=1}^{n} \sum_{j=1}^{n} c_{ij} x_i x_j + \ldots \tag{10}$$

where x_i are variables of the function and c_0, c_i and c_{ij} are tuning parameters. N is total numbers of variables. Since the number of variables and DOE elements was low, the model was able to fit the data well. However, it's important to exercise caution when using this model to predict data outside of the range of design variables. Although the R2 value of 1 suggests that the model explains all of the variability in the data that it was fit to, this doesn't necessarily guarantee that it will generalize well to new data. It's worth noting that the study was subject to strict dimensional boundaries due to design and manufacturability constraints. Therefore, the choice of 15 elements in the DOE table was deemed reasonable. However, it's important to carefully consider the choice of sample size in a DOE based on the relevant factors and research question at hand. The curve expressions were given in eqs. (11) and (12). The high-order polynomial RSM of specific energy absorption was expressed with:

$$\begin{aligned} SEA = {} & 50.186552 - 6.592871 \times x(1) + 0.008779 \times x(2) + 0.801241 \times x(3) \\ & - 72.861971 \times x(4) + 0.255839 \times x(1) \times x(1) + 0.000224 \times x(1) \\ & \times x(2) - 0.013573 \times x(1) \times x(3) + 0.099387 \times x(1) \times x(4) \\ & - 0.000399 \times x(2) \times x(2) + 0.000209 \times x(2) \times x(3) + 0.059596 \\ & \times x(2) \times x(4) - 0.004920 \times x(3) \times x(3) + 0.223660 \times x(3) \times x(4) \\ & + 28.937022 \times x(4) \times x(4) \end{aligned} \tag{11}$$

The high-order polynomial RSM of relative volume (RV) was expressed with:

$$\begin{aligned} RV = {} & -0.440240 - 0.004993 \times x(1) + 0.004033 \times x(2) + 0.031832 \times x(3) \\ & - 1.441300 \times x(4) + 0.000610 \times x(1) \times x(1) - 0.000019 \times x(1) \\ & \times x(2) - 0.000275 \times x(1) \times x(3) - 0.011983 \times x(1) \times x(4) \\ & - 0.000017 \times x(2) \times x(2) - 0.000019 \times x(2) \times x(3) + 0.000246 \\ & \times x(2) \times x(4) - 0.000162 \times x(3) \times x(3) + 0.001787 \times x(3) \times x(4) \\ & + 0.965557 \times x(4) \times x(4) \end{aligned} \tag{12}$$

where $x(1) = w_{unit}, x(2) = \theta_1, x(3) = \theta_2, x(4) = t$. The pareto optimal solutions were obtained using Non-Dominated Sorting Genetic Algorithm–II (NSGA-II). It is based on the principles of genetic algorithms (GA) and sort the population of solutions into different fronts based on their level of dominance. The algorithm works by first generating an initial population of candidate solutions, and then iteratively applying a series of genetic operations, including selection, crossover, and mutation, to generate new candidate solutions. The non-dominated sorting is then used to evaluate and select the best solutions for the next generation. The process continues until the maximum number of generations is reached. Table 9 shows NSGAII values that provide good repeatability in solutions. Readers are directed to Ref. [63]. for further details of GA. The Pareto front is a set of solutions that are non-dominated, meaning that no solution in the set is better than another solution in all objective functions simultaneously.

The obtained Pareto front is presented in Fig. 17, along with the utopia point which represents the best points for each of the target objectives. The closest point to the utopia was selected using the Euclidian distance calculation. This was repeated for different objective weights which were couples of 0.5–0.5, 0.6–0.4, and 0.4–0.6, respectively, and these were plotted in pareto front curve with red, green and pink color, respectively, as shown in Fig. 17-b. Table 10 lists obtained design parameters for each objectives set. The results show that SEA prioritized objectives ([0.6 0.4]), outputs a larger θ_2, compared to other two sets. And it has a higher relative volume than others. Three optimized parts have constant thickness of 0.6 mm and a value of θ_1 around 148°.

Table 7
Three levels variables employed in the design of experiments.

Variable	Low level	Intermediate level	High level
w_{unit} [mm]	10	12.5	16.6
θ_1 [°]	50	70	90
θ_2 [°]	100	130	150
t [mm]	0.6	0.8	1.2

Table 8
DOE table for creating a response surface.

Design no	w_{unit} [mm]	θ_1 [°]	θ_2 [°]	t [mm]	Box volume [mm^3]	Lattice volume[a] [mm^3]	Relative volume	Mass [gram]	SEA [kJ/kg]
1	16.66	150	90	0.6	49.98 × 22.83 × 25	5405	0.189	23.9	4.12
2	10	150	50	0.6	55.9 × 61.08 × 25	14506	0.165	64.3	4.43
3	10	150	90	1.2	50 × 20.58 x 25	14676	0.570	67.8	15.69
4	16.66	110	50	1.2	49.98 × 45.99 × 25	15305	0.266	65.0	3.02
5	10	110	50	0.6	55 × 48.7 × 25	14483	0.216	64.2	6.29
6	12.5	110	90	1.2	50 × 19.79 × 25	13977	0.565	61.9	11.00
7[b]	10	110	90	0.6	50 × 13.1 × 25	7355	0.450	32.6	11.11
8	16.66	150	50	1.2	49.98 × 55.78 × 25	15050	0.216	66.7	2.65
9	10	130	90	0.6	50 × 17.5 × 25	8575	0.393	38.0	11.04
10	16.66	110	90	0.6	50 × 14.5 × 25	5013	0.276	22.2	5.59
11	16.66	130	90	1.2	50 × 17.2 × 25	8876	0.413	39.3	10.27
12	12.5	150	70	0.9	50 × 35.4 × 25	12148	0.275	53.8	3.92
13	16.66	130	50	0.6	54.5 × 53 × 25	8415	0.117	37.3	3.11
14	10	130	50	1.2	50 × 52.6 × 25	24728	0.376	110.0	5.01
15	10	110	70	1.2	50 × 21.8 × 25	15940	0.584	70.6	12.39

[a] Decimals were rounded up.
[b] For DOE7, t = 0.9 mm was revised to 0.6 mm due to physical limits.

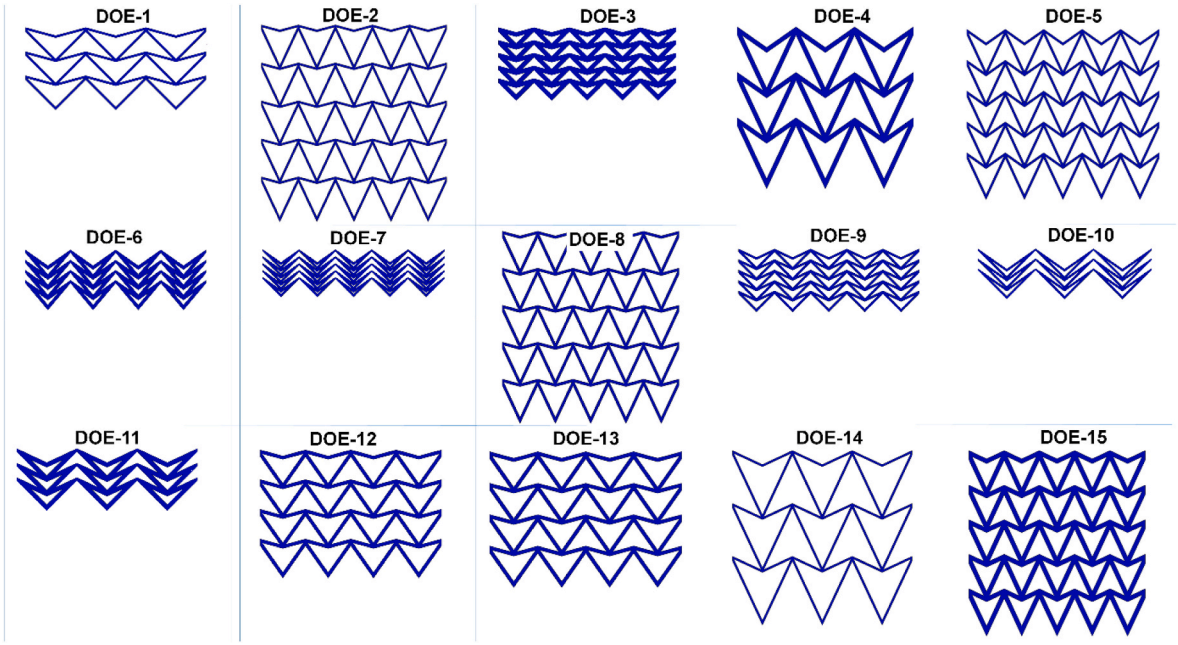

Fig. 16. Front-views of the designs in the DOE table.

Table 9
Selected optimization parameters of the NSGAII.

Population size	2000
Repository size	25
Number of generation	1000
The probability of cross-over	80 %
The probability of mutation	20 %

Table 11 lists calculated and predicted SEA and relative volume of three optimum lattice blocks. As expected, predicted SEA of optimization overestimates SEA of finite element analysis for all three optimum sets, due to many nonlinear buckling, happened during compressions. Relative volume is calculated in the design phase. Difference between predicted relative volume and CAD could arise due to nature of the method, that were varied amount of sections in the merge process of unit cells. Fig. 18 shows compressed states and resulted deformation patterns of these optimized blocks. The compression progress from the bottom towards the top as in the experiments, and the cells show early explicit deformations as the struts are thin such as 0.6 mm. Overall, the optimization succeeded in predicting SEA values that are close to the FEA results. Note that three optimum designs were obtained within the certain limits such as block width (<56 mm), linked number of columns (max 5 columns∩equal number of rows) and constant depth (25 mm). SEA and relative volume of optimized three designs are 6.95 kJ/kg −0.236, 8.36 kJ/kg-0.330 and 6.02 kJ/kg-0.215, respectively.

3.5. Outlook

After discussing the experimental results in sections 3.1 and 3.2, we note that previous studies have shown that polymeric 2D DAH lattice structures can absorb more energy compared to conventional honeycomb and 2D re-entrant lattice structures under in-plane compression loading [64]. However, to our knowledge, there has been no report investigating the response of 2D DAH lattice structures manufactured using PBF process. This study specifically aimed to address this gap by investigating the manufacturing of 2D DAH lattice structures using Ti64 and the PBF-EB process, and reporting their compressive energy absorption and failure modes. The results revealed that different scan speeds in the PBF-EB process resulted in significant variation (up to 25

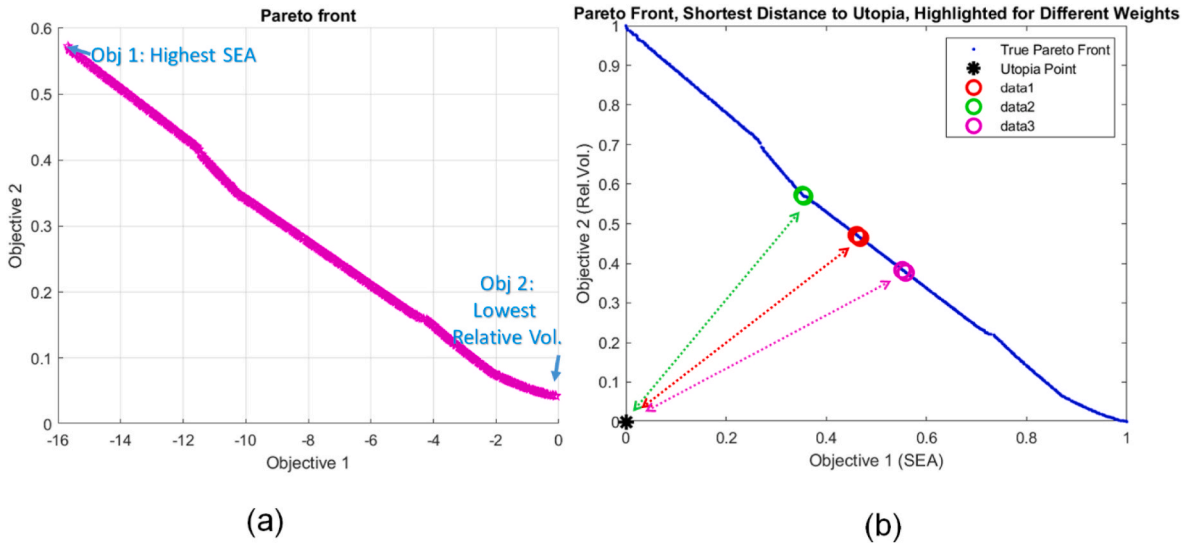

Fig. 17. Pareto front for objective 1 (SEA) and objective 2 (relative volume). representing highest and lowest values for each. (b) Normalized Pareto front with the closest points to the utopia with different weights of the objectives; [Obj1 Obj2] = [0.5 0.5] in red, [0.6 0.4] in green, [0.4 0.6] in pink, respectively.

Table 10
The design points based on the optimum objective points.

Objective weights [O1 O2]	Optimum design no	w_{unit} [mm]	θ_1 [°]	θ_2 [°]	t [mm]	Box volume [mm^3]	Lattice volume [mm^3]	Mass [gram]
[0.5 0.5]	1	10.00	148.93	65.06	0.60	50 × 34.40 × 25	10140	44.9
[0.6 0.4]	2	10.00	149.68	89.52	0.60	50 × 19.21 × 25	7927	35.1
[0.4 0.6]	3	10.00	148.67	58.46	0.60	50 × 41.21 × 25	11089	49.1

Table 11
Comparison of predicted and actual spesific energy absorption and relative volume.

	Objective weights [O1 O2]	Optimum design no	Predicted SEA [kJ/kg]	FEA SEA [kJ/kg]	Predicted relative volume	CAD relative volume
data1	[0.5 0.5]	1	8.48	6.95	0.291	0.236
data2	[0.6 0.4]	2	10.16	8.36	0.345	0.330
data3	[0.4 0.6]	3	7.07	6.02	0.243	0.215

%) in the compressive performance of them compressed at 33 % (15 mm). The amount of residual stress deployed in the lattices, number of imperfections at struts due to the three different process conditions, and weak bond between cells were identified as the main reasons for the observed differences in compressive energy absorption (e.g., less residual stress. at 45°). Additionally, this study showed that strategies lowering residual stresses at critical zones would enable to obtain higher SEA (e.g. as thin strut regions deploy more residual stress.).

Zhou et al. [64], reported SEAs of 4.2 kJ/kg and 1.1 kJ/kg for Onyx and nylon 2D DAH lattice structures, respectively. In the present study, Ti64 alloy 2D DAH lattice structures with a relative volume of 0.57 exhibited an average SEA between 8.62 kJ/kg and 11.4 kJ/kg (based on the designed mass:142.6 g, absorbed energy between 1.23 and 1.63 kJ at strain of 44 % from Table 6). In the parametric optimization for a limited design set, a DAH design with a relative volume of 0.33 absorbed 8.36 kJ/kg at a strain of 50 %. Additionally, Ti64 tensile samples manufactured in the PBF-EB process exhibited 5%–10 % failure strain which is lower comparing to that of conventional Ti64 sheet. However, when Ti64 lattice structures with fewer imperfections and a longer strain before the failure were obtained, the dissipated plastic collapse energy also increased. This study covers the results within the limits of manufacturing process (PBF-EB - 24 J/mm^3 constant beam energy density, 0°- 45° build orientations) and numerical optimization sets (four variables, two objectives with 15 elements at DOE). Different process and design sets can contribute to obtaining higher SEA values.

4. Conclusion

The study investigated compression deformation and energy absorption of Ti64 DAH lattice structures built with different beam scan speeds at various build orientations (0° and 45°). Following experimental compression tests and finite element analysis verification, a parametric optimization study was conducted. Experimental studies which are based on micro-characterization and compression tests of Ti64 2D DAH lattice structures summarized as following:

(1) KAM values showed that thin struts at unit cells accumulated more residual stress compared to thick struts due to a different number of scans during the PBF-EB process. This contributed to the initiation of failures at these locations during the compression tests (deformations).
(2) Additionally, 45° samples exhibited lower residual stresses. However, this did not create a significant difference in compression deformation patterns.
(3) Samples manufactured at low scan speeds (0deg-LS, 45deg-LS) exhibited the lowest micro-porosity, measuring at 0.12 %. Concerning the 0° built samples, it was observed that 0deg-LS exhibited slightly higher residual stresses, which were a non-comparable amount.
(4) The LS group samples exhibited the highest initial reaction peak forces compared to the HS and SF groups of both 0° and 45° built samples. The lower porosity of the LS group may be linked to these higher reaction forces, although further investigation is needed regarding the measuring the effect of the residual stress.
(5) Additionally, 0deg-LS and 45deg-LS lattice blocks absorbed the highest energy comparing to other 0deg and 45deg groups at 10

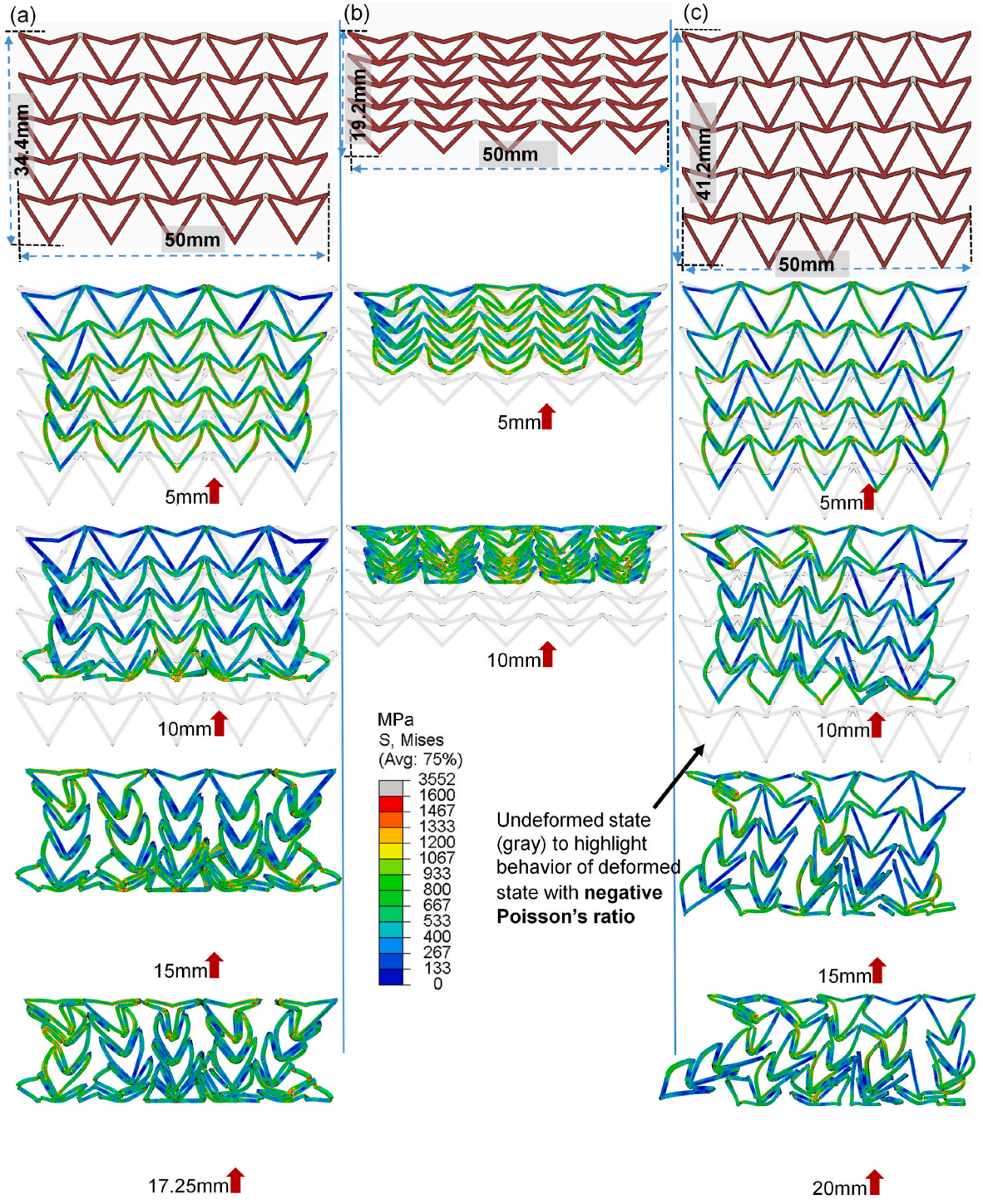

Fig. 18. Deformation patterns of optimized three 2D DAH designs listed in Table 11. (a) The design with [Obj1 Obj2] = [0.5 0.5] (b) [0.6 0.4] (c) [0.4 0.6] respectively.

mm and 15 mm, respectively. The 0deg-LS, absorbed 21.6 % and 24 % more energy than 0deg-SF (built with scan speed function) and 0deg-HS (high scan speed) samples, respectively. LS group's lower porosity contributed to having higher compressive energy absorption. As its unit cells deployed same/or slightly higher residual stress, further investigation is needed regarding the measuring the effect of the residual stress on the energy absorption.

(6) It is clearly seen that the effect of scan speed was captured strongly at 0° samples while this effect was not as pronounced for 45° samples at 15 mm.
(7) As the compressions reached towards 33 % of the height of the blocks, absorbed energies started to deviate due to many sources of random failures, which caused to separation of uncrushed pieces away during the tests.

Having verified numerical model is crucial as the weaknesses of the local areas in the manufactured lattice block can only be demonstrated

through experimental compressions. After having verified numerical models by absorbed energies and compression patterns, parametric studies showed that:

(8) Having knowledge of the effects of manufacturing on the compression numerical analyses is essential for correlating experimental deformations. In this regard, calibration, such as introducing weak zones in the compression experiments and using damage parameters, helped simulate the laying down sections in the experiments. Although it is not possible to depict the sudden detachment of uncrushed pieces in numerical analyses, pieces lying on the sides were demonstrated through numerical calibration.
(9) Parametric optimization contributed to decrease the relative volume of the lattice block in the experiments from 0.57 to 0.33 while SEA value was held close to same level in the experiments.

As a future study, numerically optimized Ti64 DAH geometries with a reduced relative volume, as presented in section 3.4, should be experimentally compressed to observe fracture-prone locations. DAH lattice structures with thinner struts, such as 0.6 mm compared to the 1 mm used in the current experiments, should be investigated to understand how varying scan speeds and build orientations are effective on the deformation pattern and energy absorption. Exploring other 2D geometries aimed at achieving higher specific energy is also of interest in order to understand their performance under different PBF-EB process conditions.

Declaration of competing interest

The authors declare that they have no known competing financial interests or personal relationships that could have appeared to influence the work reported in this paper.

Acknowledgement

The first author acknowledges the support of the Council of Higher Education of Türkiye (YÖK) as a part of the 100/2000 Doctoral Scholarship Program. This work has also been partially supported by Grants-in-Aid for Scientific Research (Grant Number: 23H00235) from the Japan Society for the Promotion of Science (JSPS), and CREST (Grant Number: JPMJCR2194) from the Japan Science and Technology Agency (JST).

Appendix A. Supplementary data

Supplementary data to this article can be found online at https://doi.org/10.1016/j.jmrt.2023.11.027.

References

[1] Evans KE. Auxetic polymers: a new range of materials. Endeavour 1991;15:170–4. https://doi.org/10.1016/0160-9327(91)90123-S.
[2] Chan N, Evans K. Indentation resilience of conventional and auxetic foams. J Cell Plast 1998;34:231–60. https://doi.org/10.1177/0021955X9803400304.
[3] Alderson KL, Evans KE. Auxetic materials: the positive side of being negative. Eng Sci Educ J 2000;9:148–54. https://doi.org/10.1049/esej:20000402.
[4] Gonella S, Ruzzene M. Homogenization and equivalent in-plane properties of two-dimensional periodic lattices. Int J Solid Struct 2008;45:2897–915. https://doi.org/10.1016/j.ijsolstr.2008.01.002.
[5] Ju J, Summers JD, Ziegert J, Fadel G. Design of honeycomb meta-materials for high shear flexure, vol. 49026; 2009. https://doi.org/10.1115/DETC2009-87730. 805–13.
[6] Tee K, Spadoni A, Scarpa F, Ruzzene M. Wave propagation in auxetic tetrachiral honeycombs. J Vib Acoust 2010;132. https://doi.org/10.1115/1.4000785.
[7] Assidi M, Ganghoffer J-F. Composites with auxetic inclusions showing both an auxetic behavior and enhancement of their mechanical properties. Compos Struct 2012;94:2373–82. https://doi.org/10.1016/j.compstruct.2012.02.026.
[8] Gohar S, Hussain G, Ilyas M, Ali A. Performance of 3D printed topologically optimized novel auxetic structures under compressive loading: experimental and FE analyses. J Mater Res Technol 2021;15:394–408. https://doi.org/10.1016/j.jmrt.2021.07.149.
[9] Sadegh Ebrahimi M, Hashemi R, Etemadi E. In-plane energy absorption characteristics and mechanical properties of 3D printed novel hybrid cellular structures. J Mater Res Technol 2022;20:3616–32. https://doi.org/10.1016/j.jmrt.2022.08.064.
[10] Yin H, Zhang W, Zhu L, Meng F, Liu J, Wen G. Review on lattice structures for energy absorption properties. Compos Struct 2023;304:116397. https://doi.org/10.1016/j.compstruct.2022.116397.
[11] Remennikov A, Kalubadanage D, Ngo T, Mendis P, Alici G, Whittaker A. Development and performance evaluation of large-scale auxetic protective systems for localised impulsive loads. Int J Prot Struct 2019;10:390–417.
[12] Qiao JX, Chen CQ. Impact resistance of uniform and functionally graded auxetic double arrowhead honeycombs. Int J Impact Eng 2015;83:47–58. https://doi.org/10.1016/j.ijimpeng.2015.04.005.
[13] Wang X-T, Wang B, Wen Z-H, Ma L. Fabrication and mechanical properties of CFRP composite three-dimensional double-arrow-head auxetic structures. Compos Sci Technol 2018;164:92–102. https://doi.org/10.1016/J.COMPSCITECH.2018.05.014.
[14] Chen Y-L, Wang X-T, Ma L. Damping mechanisms of CFRP three-dimensional double-arrow-head auxetic metamaterials. Polym Test 2020;81:106189. https://doi.org/10.1016/j.polymertesting.2019.106189.
[15] Gao Q, Ge C, Zhuang W, Wang L, Ma Z. Crashworthiness analysis of double-arrowed auxetic structure under axial impact loading. Mater Des 2019;161:22–34.
[16] Yang H, Wang B, Ma L. Mechanical properties of 3D double-U auxetic structures. Int J Solid Struct 2019;180:13–29.
[17] Yang L, Harrysson O, West H, Cormier D. Compressive properties of Ti–6Al–4V auxetic mesh structures made by electron beam melting. Acta Mater 2012;60:3370–9. https://doi.org/10.1016/j.actamat.2012.03.015.
[18] Günaydin K, Eren Z, Kazanci Z, Scarpa F, Grande AM, Türkmen HS. in-plane compression behavior of anti-tetrachiral and re-entrant lattices. Smart Mater Struct 2019. https://doi.org/10.1088/1361-665X/ab47c9.
[19] Choudhry NK, Panda B, Kumar S. In-plane energy absorption characteristics of a modified re-entrant auxetic structure fabricated via 3D printing. Compos Part B 2022;228:109437. https://doi.org/10.1016/j.compositesb.2021.109437.
[20] Guo Y, Zhang J, Chen L, Du B, Liu H, Chen L, et al. Deformation behaviors and energy absorption of auxetic lattice cylindrical structures under axial crushing load. Aero Sci Technol 2020;98:105662. https://doi.org/10.1016/j.ast.2019.105662.
[21] Wang J, Luo X, Wang K, Yao S, Peng Y. On impact behaviors of 3D concave structures with negative Poisson's ratio. Compos Struct 2022;298:115999. https://doi.org/10.1016/j.compstruct.2022.115999.
[22] Zhao Y, Deng X, Zheng S, Liu X, Wang Y. Study on quasi-static axial compression performances and energy absorption of four-star double arrow honeycomb. Compos Struct 2023:116816. https://doi.org/10.1016/j.compstruct.2023.116816.
[23] Xu M, Zhao Z, Wang P, Duan S, Lei H, Fang D. Mechanical performance of bio-inspired hierarchical honeycomb metamaterials. Int J Solid Struct 2022;254:111866. https://doi.org/10.1016/j.ijsolstr.2022.111866.
[24] Arjunan A, Singh M, Baroutaji A, Wang C. Additively manufactured AlSi10Mg inherently stable thin and thick-walled lattice with negative Poisson's ratio. Compos Struct 2020:112469. https://doi.org/10.1016/j.compstruct.2020.112469.
[25] Abd-Elaziem W, Elkatatny S, Abd-Elaziem A-E, Khedr M, Abd El-baky MA, Hassan MA, et al. On the current research progress of metallic materials fabricated by laser powder bed fusion process: a review. J Mater Res Technol 2022;20:681–707. https://doi.org/10.1016/j.jmrt.2022.07.085.
[26] Dutta B, Froes FH. The Additive Manufacturing (AM) of titanium alloys. Met Powder Rep 2017;72:96–106. https://doi.org/10.1016/j.mprp.2016.12.062.
[27] Pei E, Kabir I, Breški T, Godec D, Nordin A. A review of geometric dimensioning and tolerancing (GD&T) of additive manufacturing and powder bed fusion lattices. Prog Addit Manuf 2022;7:1297–305.
[28] Ding J, Qu S, Zhang L, Wang MY, Song X. Geometric deviation and compensation for thin-walled shell lattice structures fabricated by high precision laser powder bed fusion. Addit Manuf 2022;58:103061.
[29] Singh P, Balla VK, Tofangchi A, Atre SV, Kate KH. Printability studies of Ti-6Al-4V by metal fused filament fabrication (MF3). Int J Refract Met Hard Mater 2020;91:105249.
[30] Caminero MÁ, Romero Gutiérrez A, Chacón JM, García-Plaza E, Núñez PJ. Effects of fused filament fabrication parameters on the manufacturing of 316L stainless-steel components: geometric and mechanical properties. Rapid Prototyp J 2022;28:2004–26.
[31] Nazir A, Gokcekaya O, Billah KMM, Ertugrul O, Jiang J, Sun J, et al. Multi-material additive manufacturing: a systematic review of design, properties, applications, challenges, and 3D Printing of materials and cellular metamaterials. Mater Des 2023:111661.
[32] Wang P, Song J, Nai MLS, Wei J. Experimental analysis of additively manufactured component and design guidelines for lightweight structures: a case study using electron beam melting. Addit Manuf 2020;33:101088. https://doi.org/10.1016/j.addma.2020.101088.
[33] Vayssette B, Saintier N, Brugger C, Elmay M, Pessard E. Surface roughness of Ti-6Al-4V parts obtained by SLM and EBM: effect on the high cycle fatigue life. Procedia Eng 2018;213:89–97.
[34] Koutiri I, Pessard E, Peyre P, Amlou O, De Terris T. Influence of SLM process parameters on the surface finish, porosity rate and fatigue behavior of as-built Inconel 625 parts. J Mater Process Technol 2018;255:536–46.
[35] Chowdhury S, Yadaiah N, Prakash C, Ramakrishna S, Dixit S, Gupta LR, et al. Laser powder bed fusion: a state-of-the-art review of the technology, materials,

properties & defects, and numerical modelling. J Mater Res Technol 2022;20:2109–72. https://doi.org/10.1016/j.jmrt.2022.07.121.
[36] Lee J-R, Lee M-S, Yeon SM, Kang D, Jun T-S. Influence of heat treatment and loading direction on compressive deformation behaviour of Ti–6Al–4V ELI fabricated by powder bed fusion additive manufacturing. Mater Sci Eng, A 2022;831:142258. https://doi.org/10.1016/j.msea.2021.142258.
[37] Gong H, Rafi K, Gu H, Starr T, Stucker B. Analysis of defect generation in Ti–6Al–4V parts made using powder bed fusion additive manufacturing processes. Addit Manuf 2014;1:87–98. https://doi.org/10.1016/j.addma.2014.08.002.
[38] Luo Q, Yin L, Simpson TW, Beese AM. Effect of processing parameters on pore structures, grain features, and mechanical properties in Ti-6Al-4V by laser powder bed fusion. Addit Manuf 2022;56:102915. https://doi.org/10.1016/j.addma.2022.102915.
[39] McGregor M, Patel S, McLachlin S, Vlasea M. Architectural bone parameters and the relationship to titanium lattice design for powder bed fusion additive manufacturing. Addit Manuf 2021;47:102273. https://doi.org/10.1016/j.addma.2021.102273.
[40] de Campos Carolo L, Ordoñez REC. A review on the influence of process variables on the surface roughness of Ti-6Al-4V by electron beam powder bed fusion. Addit Manuf 2022:103103. https://doi.org/10.1016/j.addma.2022.103103.
[41] Hossain U, Ghouse S, Nai K, Jeffers JR. Controlling and testing anisotropy in additively manufactured stochastic structures. Addit Manuf 2021;39:101849. https://doi.org/10.1016/j.addma.2021.101849.
[42] Cansizoglu O, Harrysson OLA, Cormier D, West H, Mahale T. Properties of Ti–6Al–4V non-stochastic lattice structures fabricated via electron beam melting. Mater Sci Eng, A 2008;492:468–74. https://doi.org/10.1016/j.msea.2008.04.002.
[43] Xiao L, Song W, Hu M, Li P. Compressive properties and micro-structural characteristics of Ti–6Al–4V fabricated by electron beam melting and selective laser melting. Mater Sci Eng, A 2019;764:138204. https://doi.org/10.1016/j.msea.2019.138204.
[44] du Plessis A, Razavi SMJ, Berto F. The effects of microporosity in struts of gyroid lattice structures produced by laser powder bed fusion. Mater Des 2020;194:108899. https://doi.org/10.1016/j.matdes.2020.108899.
[45] Choy SY, Sun C-N, Leong KF, Wei J. Compressive properties of Ti-6Al-4V lattice structures fabricated by selective laser melting: design, orientation and density. Addit Manuf 2017;16:213–24. https://doi.org/10.1016/j.addma.2017.06.01.
[46] Ataee A, Li Y, Fraser D, Song G, Wen C. Anisotropic Ti-6Al-4V gyroid scaffolds manufactured by electron beam melting (EBM) for bone implant applications. Mater Des 2018;137:345–54. https://doi.org/10.1016/j.matdes.2017.10.040.
[47] Li P, Ma YE, Sun W, Qian X, Zhang W, Wang Z. Fracture and failure behavior of additive manufactured Ti6Al4V lattice structures under compressive load. Eng Fract Mech 2021;244:107537. https://doi.org/10.1016/j.engfracmech.2021.107537.
[48] Del Guercio G, Galati M, Saboori A. Innovative approach to evaluate the mechanical performance of Ti–6Al–4V lattice structures produced by electron beam melting process. Met Mater Int 2021;27:55–67. https://doi.org/10.1007/s12540-020-00745-2.
[49] Ikeo N, Matsumi T, Ishimoto T, Ozasa R, Matsugaki A, Matsuzaka T, et al. Fabrication of Ti-alloy powder/solid composite with uniaxial anisotropy by introducing unidirectional honeycomb structure via electron beam powder bed fusion. Crystals 2021;11:1074. https://doi.org/10.3390/cryst11091074.
[50] Kotzem D, Arold T, Bleicher K, Raveendran R, Niendorf T, Walther F. Ti6Al4V lattice structures manufactured by electron beam powder bed fusion - microstructural and mechanical characterization based on advanced in situ techniques. J Mater Res Technol 2023;22:2111–30. https://doi.org/10.1016/j.jmrt.2022.12.075.
[51] Shanbhag G, Wheat E, Moylan S, Vlasea M. Effect of specimen geometry and orientation on tensile properties of Ti-6Al-4V manufactured by electron beam powder bed fusion. Addit Manuf 2021;48:102366. https://doi.org/10.1016/j.addma.2021.102366.
[52] Radlof W, Benz C, Heyer H, Sander M. Monotonic and fatigue behavior of EBM manufactured Ti-6Al-4V solid samples: experimental, analytical and numerical investigations. Materials 2020;13:4642. https://doi.org/10.3390/ma13204642.
[53] Zhou T, Wu J, Che J, Wang Y, Wang X. Dynamic shear characteristics of titanium alloy Ti-6Al-4V at large strain rates by the split Hopkinson pressure bar test. Int J Impact Eng 2017;109:167–77. https://doi.org/10.1016/j.ijimpeng.2017.06.007.
[54] Deb S, Muraleedharan A, Immanuel R, Panigrahi S, Racineux G, Marya S. Establishing flow stress behaviour of Ti-6Al-4V alloy and development of constitutive models using Johnson-Cook method and Artificial Neural Network for quasi-static and dynamic loading. Theor Appl Fract Mech 2022;119:103338. https://doi.org/10.1016/j.tafmec.2022.103338.
[55] Damage evolution and element removal for ductile metals. Abaqus Anal Users Guide n.d. http://130.149.89.49:2080/v6.13/books/usb/default.htm?startat=pt05ch24s02abm43.html (accessed October 14, 2022).
[56] Chen G, Ren C, Yang X, Jin X, Guo T. Finite element simulation of high-speed machining of titanium alloy (Ti–6Al–4V) based on ductile failure model. Int J Adv Manuf Technol 2011;56:1027–38. https://doi.org/10.1007/s00170-011-3233-6.
[57] Dassault Systems Abaqus theory manual. 2016. http://130.149.89.49:2080/v6.11/pdf_books/THEORY.pdf. [Accessed 4 September 2022].
[58] Hernández-Nava E, Smith CJ, Derguti F, Tammas-Williams S, Leonard F, Withers PJ, et al. The effect of defects on the mechanical response of Ti-6Al-4V cubic lattice structures fabricated by electron beam melting. Acta Mater 2016;108:279–92. https://doi.org/10.1016/j.actamat.2016.02.029.
[59] Gong X, Lydon J, Cooper K, Chou K. Beam speed effects on Ti–6Al–4V microstructures in electron beam additive manufacturing. J Mater Res 2014;29:1951–9. https://doi.org/10.1557/jmr.2014.125.
[60] Zeng K, Pal D, Teng C, Stucker BE. Evaluations of effective thermal conductivity of support structures in selective laser melting. Addit Manuf 2015;6:67–73. https://doi.org/10.1016/j.addma.2015.03.004.
[61] Li Z, Xu R, Zhang Z, Kucukkoc I. The influence of scan length on fabricating thin-walled components in selective laser melting. Int J Mach Tool Manuf 2018;126:1–12. https://doi.org/10.1016/j.ijmachtools.2017.11.012.
[62] Gokcekaya O, Ishimoto T, Todo T, Suganuma R, Fukushima R, Narushima T, et al. Effect of scan length on densification and crystallographic texture formation of pure chromium fabricated by laser powder bed fusion. Crystals 2020;11:9. https://doi.org/10.3390/cryst11010009.
[63] Gen M, Cheng R. Genetic algorithms and engineering optimization, vol. 7. John Wiley & Sons; 1999.
[64] Zhou J, Liu H, Dear JP, Falzon BG, Kazanci Z. Comparison of different quasi-static loading conditions of additively manufactured composite hexagonal and auxetic cellular structures. Int J Mech Sci 2023;244:108054. https://doi.org/10.1016/j.ijmecsci.2022.108054.